

A Compton-thin Solution for the *Suzaku* X-ray Spectrum of the Seyfert 2 Galaxy Mkn 3

T. Yaqoob^{1,2}, M. M. Tatum², A. Scholtes², A. Gottlieb², T. J. Turner²

¹*Department of Physics and Astronomy, Johns Hopkins University, 3400 N. Charles St., Baltimore, MD 21218.*

²*Department of Physics, University of Maryland Baltimore County, Baltimore, MD 21250.*

Accepted 2015 August 28. Received 2015 August 27; in original form 2015 June 15

ABSTRACT

Mkn 3 is a Seyfert 2 galaxy that is widely regarded as an exemplary Compton-thick AGN. We study the *Suzaku* X-ray spectrum using models of the X-ray reprocessor that self-consistently account for the Fe $K\alpha$ fluorescent emission line and the associated Compton-scattered, or reflection, continuum. We find a solution in which the average global column density, $0.234^{+0.012}_{-0.010} \times 10^{24} \text{ cm}^{-2}$, is very different to the line-of-sight column density, $0.902^{+0.012}_{-0.013} \times 10^{24} \text{ cm}^{-2}$. The global column density is ~ 5 times smaller than that required for the matter distribution to be Compton-thick. Our model accounts for the profiles of the Fe $K\alpha$ and Fe $K\beta$ lines, and the Fe K edge remarkably well, with a solar abundance of Fe. The matter distribution could consist of a clumpy medium with a line-of-sight column density higher than the global average. A uniform, spherically-symmetric distribution alone cannot simultaneously produce the correct fluorescent line spectrum and reflection continuum. Previous works on Mkn 3, and other AGN, that assumed a reflection continuum from matter with an infinite column density could therefore lead to erroneous or “puzzling” conclusions if the matter out of the line-of-sight is really Compton-thin. Whereas studies of samples of AGN have generally only probed the line-of-sight column density, with simplistic, one-dimensional models, it is important now to establish the global column densities in AGN. It is the global properties that affect the energy budget in terms of reprocessing of X-rays into infrared emission, and that constrain population synthesis models of the cosmic X-ray background.

Key words: galaxies: active - galaxies: individual (Mkn 3) - radiation mechanisms: general - scattering - X-rays: general

1 INTRODUCTION

The circumnuclear matter surrounding the putative supermassive accreting black hole in active galactic nuclei (AGNs), thought to be responsible for obscuration of the primary continuum emission in type 2 AGNs, also plays a critical role in accounting for the shape of the cosmic X-ray background spectrum, or CXRB (e.g. Gilli, Comastri & Hasinger 2007; Ueda et al. 2014). In recent years, much emphasis has been placed upon Compton-thick AGNs, formally defined by an optical depth to electron scattering in the Thomson limit that is greater than unity ($N_{\text{H}} > (1.2\sigma_{\text{T}})^{-1}$, or $1.25 \times 10^{24} \text{ cm}^{-2}$). Although this value of N_{H} is arbitrary in terms of the effects of photoelectric absorption, Compton scattering, and the prominence of the ubiquitous Fe $K\alpha$ emission line, the distinction separates sources in which the mean number of scatterings per photon is less than or greater than one (for Compton-thin and Compton-thick sources respectively). Strictly speaking, the Compton-thick definition should also be energy-dependent, but the conventional use of the term in the literature ignores this, so the conventional use implicitly refers to the low-energy limit, when the Klein-Nishina cross-section is equal to the Thomson cross-section. With these caveats, it is generally thought that Compton-thick AGNs could constitute 50% or more of the obscured AGN population that contributes to the CXRB (e.g. Gilli et al. 2007; Ueda et al. 2014, and references therein).

In type 1 AGNs the same circumnuclear matter distribution can imprint signatures of Compton scattering (reflection)

and fluorescent line emission on the observed X-ray continuum. Such a scenario is in line with AGN unification schemes, in which the line-of-sight to type 1 AGN is unobscured due to the geometry of the circumnuclear matter (e.g. Antonucci & Miller 1985; Antonucci 1993; Urry & Padovani 2005). Regardless of AGN classification, the gas and dust can reprocess the impinging intrinsic X-ray continuum into infrared emission (e.g. Elitzur 2008; Yaqoob & Murphy 2011a; Georgantopoulos et al. 2011). Hereafter, we refer to the circumnuclear matter as the X-ray reprocessor.

Using X-ray spectroscopy to infer the properties of the X-ray reprocessor in AGNs is thus important, yet it has not been fully exploited. This is because models used to fit the data have traditionally been over-simplistic, employing ad hoc components that do not self-consistently account for the Fe $K\alpha$ line emission and Compton-scattered continuum. Instead of producing the Fe $K\alpha$ line and reflection continuum in finite column density material (such as that detected in the line-of-sight), material out of the line-of-sight was modeled using a slab with an infinite column density, with an inclination angle relative to the observer fixed at an arbitrary value. Such models cannot therefore be used to *measure* the average global column density out of the line-of-sight, because the starting premise is that it is Compton-thick, without compelling justification. A good fit to the data with these models does not imply uniqueness.

Ideally, one would like to make no assumptions about the global column density of the reprocessor, and use the data to constrain the allowed values, including the “pure reflection” spectrum case (i.e. reflection from infinitely-thick matter) as a limiting form of a more general model. Such physically-motivated models that self-consistently treat the Compton-reflection and Fe $K\alpha$ fluorescent emission-line for finite column density matter, and that can be directly fitted to X-ray data, have recently been introduced and applied (e.g. Ikeda, Awaki, & Terashima 2009; Murphy & Yaqoob 2009; Brightman & Nandra 2011; Tatum et al. 2013; Liu & Li 2014). As well as fitting data from new X-ray observations (e.g. LaMassa et al. 2014; Brightman et al. 2015), it is fruitful to re-examine archival data to investigate to what extent previous conclusions change.

Compton reflection from finite column density matter produces a rich variety of possible spectra (that depend on geometry and viewing angle, as well as column density), and can be very different to the X-ray reflection spectrum from an infinite column density slab (e.g. see Ikeda et al. 2009; Murphy & Yaqoob 2009; Brightman & Nandra 2011; Liu & Li 2014). In particular, the so-called “Compton hump,” is no longer confined to the energy range of $\sim 10 - 30$ keV because the peak energy of the reflection spectrum depends on column density and geometry. In addition, the Fe abundance, which is often inferred from comparison of the Fe K edge in the reflection spectrum and the data, is subject to change, once the column density of the reflector is allowed to be finite and free. Intrinsic inferred luminosities are also subject to revision. Overall, the improved methodology allows one to probe the three-dimensional structure of the X-ray reprocessor in a unified way, as opposed to a disjoint view afforded by one-dimensional partial covering models, combined with reflection from an infinite column density slab with an arbitrary orientation relative to the observer. Indeed, the term “Compton-thick” now becomes even more ambiguous, as one should specify, for a particular AGN, whether the term refers to the line-of-sight column density, or to the average column density of the global matter distribution out of the line-of-sight, or both.

The Seyfert 2 galaxy Mkn 3, which is nearby at $z = 0.013509$ (Tift & Cocke 1988), has been well-studied across the electromagnetic spectrum. It is prototypical of its class, in that the optical broad emission lines are only seen in polarized light (Miller & Goodrich 1990; Tran 1995). Mkn 3 has been a target of all major X-ray astronomy missions since *EXOSAT*, and it is currently regarded in the literature as an archetypal Compton-thick AGN.

High spectral-resolution grating studies with *Chandra* (Sako et al. 2000), and *XMM-Newton* (Pounds et al. 2005; Bianchi et al. 2005) have established an extremely complex soft X-ray spectrum (below ~ 2 keV), rich with emission lines due predominantly to photoionized gas covering a broad range of ionization states. Hard X-ray spectra of Mkn 3 obtained with *ASCA* (Iwasawa et al. 1994; Griffiths et al. 1998), *BeppoSAX* (Cappi et al. 1999), *XMM-Newton* (Pounds et al. 2005; Bianchi et al. 2005; Akylas, Georgantopoulos, & Nandra 2006; Guainazzi et al. 2012), *Swift* (Guainazzi et al. 2012), and *Suzaku* (Awaki et al. 2008; Fukazawa et al. 2011) were all interpreted using a similar model, consisting of line-of-sight absorption and scattering, along with an X-ray reflection continuum formed in an infinite column density slab of neutral material. The prominent Fe $K\alpha$ line was modeled with an ad hoc Gaussian component. *Chandra* high spectral resolution grating data (Shu, Yaqoob, & Wang 2011) provided the best evidence that the Fe $K\alpha$ line originates in neutral matter. Shu et al. (2011) also measured a width of 3140_{-660}^{+870} km s $^{-1}$ FWHM for the Fe $K\alpha$ line, establishing the size of the line emitter to be ~ 4 times larger than the optical BLR (but smaller than the warm, photoionized region contributing to the soft X-ray spectrum). The line-of-sight column density was $\sim 10^{24}$ cm $^{-2}$ in all of the observations. Thus, whilst the nearly Compton-thick column density of the line-of-sight absorption was fairly robust because it does not depend on the geometry of the reprocessor, the Compton-thick nature of the *global* matter distribution was an assumption, not an inference.

The ad hoc treatment of the Fe $K\alpha$ line in previous studies also lead to some anomalous results that were deemed “puzzling.” For example, Guainazzi et al. (2012) found in a variability study that the Fe $K\alpha$ line flux was uncorrelated with the X-ray reflection continuum, yet the two emission components are physically related, implying that the model is incomplete. Another example is the Compton shoulder to the Fe $K\alpha$ line (due to scattered line photons), whose strength relative to the line core depends on the column density and geometry of the line emitter (e.g. see Matt 2002; Yaqoob & Murphy 2010). Using a nonphysical (Gaussian) model of the Compton shoulder, Pounds et al. (2005) forced insertion of a Compton shoulder that would be expected from the infinite column density slab that produces the reflection continuum in their model, at the

expense of distorting the centroid of the line core. They found that the peak of the Fe K α line core increased by ~ 30 eV to 6.43 ± 0.01 keV, and they estimated the ratio of the flux in the Compton shoulder to that in the core to be $\sim 20\%$. However, they also stated that adding the Compton shoulder did not result in a statistically significant improvement to the fit. This lack of a compelling Compton shoulder is only puzzling if the reflection continuum is modeled as originating in Compton-thick matter. However, such a choice for the reflection continuum is an assumption, not an inference. Indeed, none of the above anomalies can ever arise if self-consistent, finite column density models of the X-ray reprocessor are employed, because the reflection continuum and the Fe K α line, including its Compton shoulder, are all self-consistently determined from the outset. Moreover, the Compton-thick limit can be included in such models. Ikeda et al. (2009) did attempt to fit the *Suzaku* Mkn 3 spectrum with a self-consistent toroidal model. However, their model was based on Monte Carlo calculations with insufficient statistical quality to properly perform χ^2 minimization and statistical error analysis, so they were not able to derive robust constraints on the global matter distribution. They obtained a line-of-sight column consistent with previous studies, and were able to fit the data with a Compton-thick global matter distribution, but they could not rule out smaller column densities for the matter out of the line-of-sight.

Thus, it is in the context described above that we re-examine the *Suzaku* X-ray spectrum of Mkn 3, using the X-ray reprocessor models of Murphy & Yaqoob (2009), and Brightman & Nandra (2011), which overcome the limitations of previous spectral-fitting analyses. Amongst the historical X-ray data sets, the *Suzaku* data are best suited for studying the X-ray reprocessor because the instrumentation simultaneously covers the critical Fe K band ($\sim 6 - 8$ keV) with good spectral resolution and throughput (due to the XIS CCD detectors), and the hard X-ray band above 10 keV with good sensitivity. The simultaneous broadband coverage helps to reconcile the absorbed and reflected continua with the Fe K α line emission.

The paper is organized as follows. In §2 we describe the basic data, and reduction procedures. In §3 we describe the overall strategy of the analysis that we will present, including detailed procedures for setting up the various X-ray reprocessing models for spectral fitting. In §4 we give the results from fitting different X-ray reprocessor models that correspond to very distinct physical scenarios, using only data above 2.4 keV. In §5 we present the results of extending the bandpass to include the soft X-ray spectrum down to ~ 0.5 keV, using the best model fitted to the high-energy data. In §6 we summarize our results and conclusions.

2 *Suzaku* OBSERVATION AND DATA REDUCTION

The present study pertains to an observation of Mkn 3 made by the joint Japan/US X-ray astronomy satellite, *Suzaku* (Mitsuda et al. 2007) in 2005, October 22. *Suzaku* carries four X-ray Imaging Spectrometers (XIS – Koyama et al. 2007) and a collimated Hard X-ray Detector (HXD – Takahashi et al. 2007). Each XIS consists of four CCD detectors at the focal plane of its own thin-foil X-ray telescope (XRT – Serlemitsos et al. 2007), and has a field-of-view (FOV) of $17.8' \times 17.8'$. One of the XIS detectors (XIS1) is back-side illuminated (BI) and the other three (XIS0, XIS2, and XIS3) are front-side illuminated (FI). The bandpass of the FI detectors is $\sim 0.4 - 12$ keV and $\sim 0.2 - 12$ keV for the BI detector. The useful bandpass depends on the signal-to-noise ratio of the source since the effective area is significantly diminished at the extreme ends of the operational bandpasses. Although the BI CCD has higher effective area at low energies, the background level across the entire bandpass is higher compared to the FI CCDs. The HXD consists of two non-imaging instruments (the PIN and GSO – see Takahashi et al. 2007) with a combined bandpass of $\sim 10 - 600$ keV. Both of the HXD instruments are background-limited, more so the GSO, which has a smaller effective area than the PIN. For AGNs, the source count rate is typically much less than the background and in the present study we used only the PIN data, as the GSO data did not provide a reliable spectrum. In order to obtain a background-subtracted spectrum, the background spectrum must be modeled as a function of energy and time. The background model for the HXD/PIN has an advertised systematic uncertainty of 1.3%¹. However, the signal is background-dominated, and the source count rate may be a small fraction of the background count rate, so the net systematic error in the background-subtracted spectra could be significant. The observation of Mkn 3 was optimized for the HXD in terms of positioning the source at the aim point for the HXD (the so-called “HXD-nominal pointing”) which gives a somewhat lower count-rate in the XIS than the “XIS-nominal” pointing, but gives $\sim 10\%$ higher HXD effective area.

The principal data selection and screening criteria for the XIS were the selection of only *ASCA* grades 0, 2, 3, 4, and 6, the removal of flickering pixels with the FTOOL `cleansis`, and exclusion of data taken during satellite passages through the South Atlantic Anomaly (SAA), as well as for time intervals less than 256 s after passages through the SAA, using the `T_SAA.HXD` house-keeping parameter. Data were also rejected for Earth elevation angles (ELV) less than 5° , Earth day-time elevation angles (`DYE_ELV`) less than 20° , and values of the magnetic cut-off rigidity (`COR`) less than 6 GeV/ c^2 . Residual uncertainties in the XIS energy scale are on the order of 0.2% or less (or ~ 13 eV at 6.4 keV – see Koyama et al. 2007). The cleaning and data selection resulted in net exposure times that are reported in Table 1.

We extracted XIS spectra of Mkn 3 by using a circular extraction region with a radius of $3.5'$. Background XIS spectra were

¹ <http://heasarc.gsfc.nasa.gov/docs/suzaku/analysis/pinbgd.html>

Table 1. Exposure times and count rates for the *Suzaku* spectra

Detector	Exposure (ks)	Energy Range (keV)	Rate ^a (count s ⁻¹)	Percentage of on-source rate ^b
XIS	87.7	0.5–1.5, 2.4–9.3	0.1739 ± 0.0008	90.4%
PIN	85.5	14.0–45.0	0.1462 ± 0.0025	29.8%

^a Background-subtracted count rate in the energy bands specified. For the XIS, this is the rate per XIS unit, averaged over XIS0, XIS1, XIS2, and XIS3. ^b The background-subtracted source count rate as a percentage of the total on-source count rate, in the utilized energy intervals.

made from off-source areas of the detector, after removing a circular region with a radius of 4.5' centered on the source, and the calibration sources (using rectangular masks). The XIS spectra from all four detectors (XIS0, XIS1, XIS2, and XIS3) were combined into a single spectrum for spectral fitting. Instrument response matrix functions (RMF) and the ancillary response functions (ARF) were made and combined into a single response file using standard procedures (e.g. see appendix of Yaqoob, 2012). The background subtraction method for the HXD/PIN used the file `ae100040010_hxd_pinbgd.evt`, corresponding to the “tuned” version of the background model²,

It has been known since *ROSAT* observations of Mkn 3 that there is a contaminating source, IXO 30, just 1.6' away (Turner, Urry, & Mushotzky 1993; Morse et al. 1995; Colbert & Ptak 2002). The source has no optical counterpart identification and its distance is unknown. It is too close to Mkn 3 to exclude in the *Suzaku* data, since the PSF has a half-power diameter that is comparable to the separation of Mkn 3 and IXO 30. Bianchi et al. (2005), using *XMM-Newton* data, established that IXO 30 is not variable and contributed only 7% of the total flux in the 0.4–2 keV band (with a power-law photon index of 1.77). Since our spectral analysis for Mkn 3 is not focussed on the soft X-ray spectrum, this level of contamination will not have an impact on our conclusions.

The energy bandpass used for the spectrum from each instrument was determined by the systematics of the background subtraction. For the XIS, the bandpass 0.53–9.3 keV was used, for which the background was less than 50% of the source counts in any spectral bin, and in the range 0.65–8.45 keV the background never exceeded 25% of the source counts in any spectral bin. The width of the bins for the XIS data was 30 eV up to 8.0 keV, and 60 eV above 8 keV. With this spectral binning, all bins in the 0.53–9.30 keV range had greater than 20 counts, enabling the use of the χ^2 statistic for spectral fitting. (We avoid grouping spectral bins using a signal-to-noise ratio threshold because it can “wash out” absorption features.) In addition to omitting data on the basis of background-subtraction systematics, we also omitted some spectral data that are subject to calibration uncertainties in the effective area due to certain atomic features. It is known that the effective area calibration is poor in the ranges $\sim 1.8 - 1.9$ keV (due to Si in the detectors) and $\sim 2.0 - 2.4$ keV (Au M edges due to the telescopes). The effective area also has a significant, steep change at ~ 1.56 keV (due to Al in the telescopes). Given that the Mkn 3 spectrum below ~ 2 keV is rich with line emission (e.g. Sako et al. 2000; Pounds et al. 2005; Bianchi et al. 2005), making interpretation of modeling in the regions of calibration uncertainties difficult, we took the conservative approach of omitting XIS data in the 1.50–2.4 keV band for the purpose of spectral fitting. For the HXD/PIN, negative counts in the background-subtracted spectral bins clearly indicate a breakdown of the background model. We found that the spectral data in the energy range 14.25–45.0 keV produced greater than 20 counts per bin (after background subtraction), for bin widths of 0.375 keV below 35.0 keV and 0.75 keV above 35 keV. This gives the most reliable HXD/PIN spectrum with minimal binning whilst at the same time qualifying the spectrum for spectral fitting using the χ^2 statistic. The final energy ranges selected for spectral fitting for each instrument are summarized in Table 1, along with the corresponding count rates.

The calibration of the relative cross-normalizations of the XIS and PIN data involves many factors, and these have been discussed in detail in the appendix of Yaqoob (2012). For the present *Suzaku* observation of Mkn 3 we have found it to be adequate to simply use the value of the PIN:XIS ratio, $C_{\text{PIN:XIS}}$, recommended by the *Suzaku* Guest Observer Facility (GOF), which for HXD-nominal observations is $C_{\text{PIN:XIS}} = 1.18^3$.

3 ANALYSIS STRATEGY AND SPECTRAL FITTING

In Fig. 1 we show the unfolded *Suzaku* XIS and PIN spectra of Mkn 3 compared to a simple power-law continuum with an arbitrary normalization, and photon index, Γ , of 1.8 (a value typical of the intrinsic continuum of Seyfert galaxies in the pertinent energy range). The actual values of the normalization and Γ are not important here because the purpose of the plot

² See <http://heasarc.gsfc.nasa.gov/docs/suzaku/analysis/pinbgd.html>

³ <ftp://legacy.gsfc.nasa.gov/suzaku/doc/xrt/suzakumemo-2008-06.pdf>

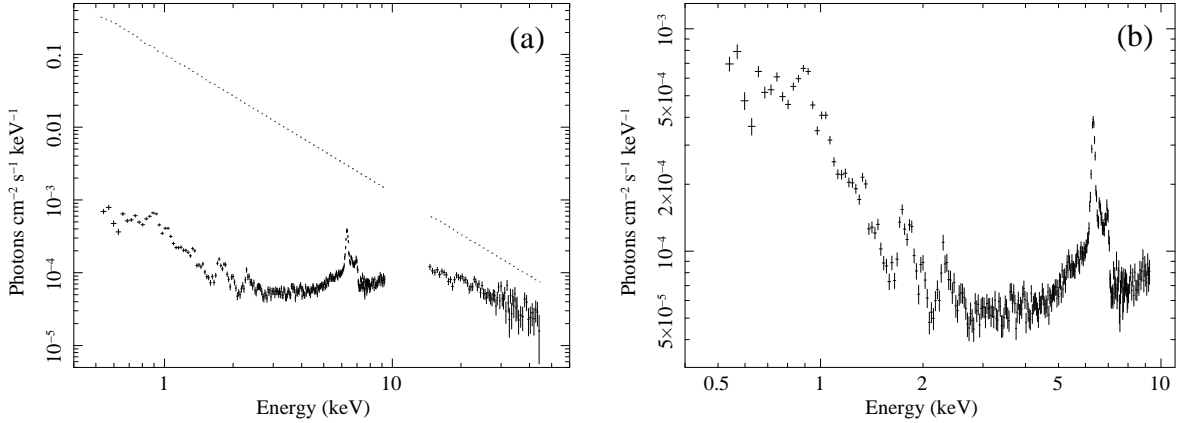


Figure 1. (a) The unfolded *Suzaku* XIS and PIN spectra of Mkn 3, compared to a power-law with a photon index of 1.8 (dotted line). The data below and above 10 keV are from the XIS and PIN respectively, and the data from XIS0, XIS1, XIS2, and XIS3 are combined. It can be seen that absorption and X-ray reprocessing causes the overall spectrum above 2 keV to be very flat. (b) The same spectrum as in (a), zoomed in on the XIS data.

is simply to show the salient characteristics of the overall spectrum. Full spectral-fitting will then yield the actual parameters of the intrinsic continuum. It can be seen from Fig. 1 that above ~ 2 keV the spectrum is very flat due to absorption and reflection, and there is complex structure around the Fe $K\alpha$ emission line in the ~ 6 – 8 keV Fe K band. The spectrum steepens towards low energies and below ~ 3 keV there are many emission and absorption features, which have been well-studied with both CCD and higher spectral resolution instrumentation (Sako et al. 2000; Pounds et al. 2005; Bianchi et al. 2005; Awaki et al. 2008).

The primary goal of the present spectral-fitting analysis is to determine constraints on both the line-of-sight and global column densities of matter surrounding the X-ray source, by modeling the Fe $K\alpha$ line emission self-consistently with respect to the continuum characteristics associated with X-ray absorption and reflection. The low-energy data are generally not sensitive to column densities that are large enough to produce the observed Fe $K\alpha$ line emission, because the absorbed continuum is suppressed at low energies and the data there are dominated by other emission components. Therefore we take the approach of first performing preliminary spectral modeling of the data only above 2.4 keV, which avoids the complex spectral features at soft X-ray energies, and also avoids the poor calibration of the *Suzaku* telescope effective area in the region of the Au M-edges (~ 2 – 2.4 keV). After exploring different models of the X-ray reprocessor based on these high-energy fits, we then take the best-fitting model and apply it to the full bandpass (excluding the 2–2.4 keV band containing the Au M edges), and show that we obtain column densities that are consistent with those obtained from the high-energy fits that only used data above 2.4 keV. As well as the column densities, we will show that our inferences about the constraints on the geometrical configuration of the matter distribution around the X-ray source in Mkn 3 are also consistent between the high-energy and full-bandpass fits.

For all of the models that we applied to the data, we used a simple power law for the intrinsic continuum, with the photon index (Γ) and normalization free parameters. In the high-energy fits we do not of course need to model the extremely complex soft X-ray emission. However, in Mkn 3, as is often required for many other type 2 AGNs, there is a nonthermal continuum component that is due to scattering in an extended, optically-thin region, which carries up to a few percent of the luminosity of the intrinsic continuum. We modeled this optically-thin scattered continuum with a power-law continuum that has the same photon index as the intrinsic power law. We introduce a parameter f_s , which is the fraction of the intrinsic power-law normalization that corresponds to the normalization of this scattered component. In the optically-thin limit, f_s is equal to the fraction of photons that are scattered, which in turn is approximately equal to the product of the scattering optical depth and fraction of the solid angle subtended by the material at the source that is exposed to the intrinsic X-ray continuum and visible to the observer. We will refer to the continuum associated with f_s as the “distant scattering continuum.”

We did not apply a high-energy cutoff in the form of an exponential diminishing factor that is often used, because such a form is unphysical. The X-ray reprocessor models that we use instead have a termination energy for the incident continuum (the value depends on the model used and will be given case-by-case). This is a closer approximation to actual X-ray spectra formed by Comptonization, which are characterized by a power law with a single slope up to some energy, followed by a rollover, as opposed to the continuous change in slope of exponential cutoff models. Moreover, the *Suzaku* HXD/PIN spectrum for Mkn 3 only has useful data extending to ~ 45 keV (see Fig. 1), so steepening of the high-energy continuum is not easily discernible, especially given the fact that the X-ray reprocessor models themselves cause their own high-energy steepening of the observed spectra, due to Compton downscattering in the circumnuclear matter. From *BeppoSAX* observations of Mkn 3, Cappi et al. (1999) found no evidence for a break in the spectrum up to 150 keV. Therefore, the use

of a Comptonization model for the intrinsic continuum is not necessary. However, it is important to note that whatever the form of the intrinsic continuum, in the model, that continuum must extend to higher energies than the highest energy of the data, because high-energy photons can be downscattered (many times if the medium is Compton-thick) to within the range of the data bandpass, contributing to the observed continuum, as well as to fluorescent line emission.

We used XSPEC (Arnaud 1996)⁴ for spectral fitting and utilized the χ^2 statistic for minimization. We included Galactic absorption with a column density of $8.70 \times 10^{20} \text{ cm}^{-2}$ (Stark et al. 1992) in all of the model fits described hereafter, even though it has a negligible effect for the spectral fits above 2.4 keV. For all absorption components including the Galactic one, we used photoelectric cross sections given by Verner et al. (1996). Element abundances from Anders & Grevesse (1989) were used throughout. All astrophysical model parameter values will be given in the rest frame of Mkn 3 unless otherwise stated. For the sake of brevity, certain quantities and details pertaining to particular spectral fits will be given in the tables of results and not repeated again in the text, unless it is necessary. Specifically, we are referring to the number of free parameters in a fit, the number of degrees of freedom, and the null hypothesis probability. Statistical errors given will be for one-parameter, 90% confidence (corresponding to a $\Delta\chi^2$ criterion of 2.706).

In a given energy band in the observed frame, observed fluxes will be denoted by F_{obs} , and observed (rest-frame) luminosities will be denoted by L_{obs} . These quantities are not corrected for absorption nor Compton scattering in either the line-of-sight material, or in the circumnuclear material. On the other hand, intrinsic luminosities, denoted by L_{intr} will be corrected for absorption and X-ray reprocessing, and the energy band associated with a particular value of L_{intr} will refer to the energy range in the rest frame of the source. We use a standard cosmology of $H_0 = 70 \text{ km s}^{-1} \text{ Mpc}^{-1}$, $\Lambda = 0.73$, $q_0 = 0$ throughout the paper.

3.1 Uniform Spherical Model

Here we summarize the parameters of the uniform, spherical (fully covering) X-ray reprocessor model of Brightman and Nandra (2011; hereafter BN11), implemented using the XSPEC emission table (“atable”) `sphere0708.fits` (see BN11 for details of this table). The table was explicitly calculated by BN11 for an incident power-law continuum, with a termination energy of 500 keV. The BN11 spherical model is characterized by the power-law continuum photon index (Γ) and normalization, a radial column density, (N_{H}), and two parameters that control the abundances of elements relative to solar. We call the two parameters X_{Fe} and X_{M} , where the former is the Fe abundance relative to the adopted solar value, and the latter is a single abundance multiplier for C, O, Ne, Mg, Si, S, Ar, Ca, Cr, and Ni relative to their respective solar values. The solar abundances adopted in the BN11 spherical model are those of Anders & Grevesse (1989) and the photoelectric absorption cross-sections are those of Verner et al. (1996). In all of the applications described in the present paper, we set $X_{\text{M}} = 1.0$. The BN11 spherical model self-consistently calculates the fluorescent $K\alpha$ emission lines of all of the above-mentioned elements, as well as the Fe $K\beta$ line. One restriction of the BN11 spherical model is that the emission lines cannot be separated from continuum components, and in particular, neither the Compton-scattered continuum nor the fluorescent line spectrum can be varied with respect to the directly absorbed, line-of-sight (zeroth-order) continuum. A consequence of this is that any time delays between variations in the direct continuum and the reprocessed emission from the global matter distribution (i.e. the fluorescent line emission and Compton-scattered continuum), cannot be accommodated by the model.

3.2 The MYTORUS Model

The toroidal X-ray reprocessor model, MYTORUS, has been described in detail in Murphy & Yaqoob (2009) and Yaqoob & Murphy (2010). The baseline geometry consists of a torus with a circular cross section, whose diameter is characterized by the equatorial column density, N_{H} . The torus is illuminated by a central, isotropic X-ray source, and the global covering factor of the reprocessor is 0.5, corresponding to a solid angle subtended by the structure at the central X-ray source of 2π (which in turn corresponds to an opening half-angle of 60°). The MYTORUS model self-consistently calculates the Fe $K\alpha$ and Fe $K\beta$ fluorescent emission-line spectrum and the effects of absorption and Compton scattering on the X-ray continuum and line emission. As in the case of the BN11 spherical model, the element abundances in the MYTORUS model are those of the solar values of Anders & Grevesse (1989), and the photoelectric absorption cross-sections are those of Verner et al. (1996). However, currently, none of the element abundances can be varied in the MYTORUS model.

The practical implementation of the MYTORUS model allows free relative normalizations between different components of the model in order to accommodate for differences in the actual geometry pertinent to the source (compared to the specific model assumptions used in the original calculations), and for time delays between direct continuum, Compton-scattered continuum, and fluorescent line photons⁵. The zeroth-order continuum component of the model is the direct, line-of-sight

⁴ <http://heasarc.gsfc.nasa.gov/docs/xanadu/xspec/>

⁵ See <http://mytorus.com/manual/> for details

observed continuum, and is diminished compared to the incident X-ray continuum by absorption and Compton-scattering into directions away from the line-of-sight. It is essentially a multiplicative factor that is independent of the geometry, and independent of the intrinsic continuum. This multiplicative factor is implemented with a single XSPEC table for all applications of the model (it is `mytorus_ezero_v00.fits`). The Compton-scattered continuum is implemented as an XSPEC additive table model. We used the table `mytorus_scatteredH200_v00.fits`, which corresponds to a power-law incident continuum with a termination energy of 200 keV, and a photon index (Γ) in the range 1.4–2.6. The Fe $K\alpha$ and Fe $K\beta$ emission lines are implemented with another (single) XSPEC additive table model that is produced from the same self-consistent Monte Carlo calculations that were used to calculate the corresponding Compton-scattered continuum table (we used the table `mytl_V000010nEp000H200_v00.fits`). The parameters for each of the three tables are the normalization of the incident power-law continuum (A_{PL}), Γ , N_{H} , θ_{obs} , and the redshift (z).

We denote the relative normalization between the scattered continuum and the direct, or zeroth-order continuum, by A_S , which has a value of 1.0 for the assumed geometry. This value also implies that either the intrinsic X-ray continuum flux is constant, or, for a variable intrinsic X-ray continuum, that the X-ray reprocessor is compact enough for the Compton-scattered flux to respond to the intrinsic continuum on timescales much less than the integration time for the spectrum. Conversely, departures from $A_S = 1.0$ imply departure of the covering factor from 0.5, or time delays between the intrinsic and Compton-scattered continua, or both. However, it is important to note that A_S is *not* simply related to the covering factor of the X-ray reprocessor because the detailed shape of the Compton-scattered continuum varies with covering factor. Analogously to A_S , the parameter A_L is the relative normalization of the Fe $K\alpha$ line emission, with a value of 1.0 having a similar meaning to that for $A_S = 1.0$. In our analysis we will set $A_L = A_S$ (relaxing this assumption would imply significant departure from the default model, such as non-solar Fe abundance). In practice, A_S and A_L are each implemented in XSPEC by a “constant” model component that multiplies the Compton-scattered continuum and fluorescent line table respectively.

The MYTORUS model can be applied in a number of ways that have been detailed in Yaqoob (2012), and LaMassa et al. (2014). In the simplest mode of application of the MYTORUS model, referred to as “coupled mode” (regardless of the form of the intrinsic continuum), the angle made by the axis of the torus with the observer’s line-of-sight (θ_{obs}) is coupled to the column density that is intercepted by the zeroth-order continuum. In other words, the effective geometry of the X-ray reprocessor is *precisely* that assumed in the original Monte Carlo calculations (Murphy & Yaqoob 2009), and all of the corresponding parameter values in the three MYTORUS tables are tied together. However, it is possible to apply the model in ways (described below) that mimic scenarios that have more complex geometries than that for the default, baseline assumptions.

In reality, the geometry of the circumnuclear structure in the source, particularly at the edges, may not be well represented by the exact geometry that is assumed for a specific model. In Yaqoob (2012) we showed how the MYTORUS can be used in a “decoupled mode,” to crudely mimic different geometries, by decoupling the zeroth-order continuum from the inclination angle (θ_{obs}). Since the zeroth-order continuum is independent of geometry (being purely a line-of-sight quantity), the inclination angle associated with this component becomes a dummy parameter and it is fixed at 90° so that the column density intercepting the zeroth-order continuum is literally equal to the value of the MYTORUS equatorial model column density. (In the coupled mode, the equatorial N_{H} is not equal to the line-of-sight column density for general values of θ_{obs} .) The inclination angle for the Compton-scattered continuum table can be interpreted as characterizing the Compton-scattered (or reflected) continuum in terms of the relative direction of the incident continuum source. For example, regardless of the detailed geometry, “back-side” reflection, whereby the intrinsic X-ray source lies between the observer and the reflecting material, is well-characterized by the “face-on” ($\theta_{\text{obs}} = 0^\circ$) Compton-scattered spectrum. On the other hand, if the absorbing/scattering material lies inbetween the intrinsic X-ray source and the observer, regardless of the detailed geometry, the observed spectrum is well-characterized by the “edge-on” ($\theta_{\text{obs}} = 90^\circ$) Compton-scattered spectrum (see Yaqoob, 2012). The reflected spectrum becomes less sensitive to θ_{obs} as the column density of the reflecting matter decreases, and in the optically-thin limit the spectra for $\theta_{\text{obs}} = 0^\circ$ and $\theta_{\text{obs}} = 90^\circ$ are identical. Typically, for the purpose of fitting data, the simplest scenarios should be tried first by fixing θ_{obs} at 0° and then at 90° , to determine whether the spectrum can be fitted with a dominant reflection continuum corresponding to these extremes, or a combination of them. As an example, $\theta_{\text{obs}} = 0^\circ$ might correspond to a spectrum reflected from the “far-side” of a patchy matter distribution that is observed through “holes” in the observer’s near-side of the distribution. (See, for example, Liu & Li (2014), who describe Monte Carlo simulation results for a patchy/clumpy X-ray reprocessor: a spectral-fitting model is not publicly available, however.) On the other hand, $\theta_{\text{obs}} = 90^\circ$ corresponds to a scenario in which the X-ray source is embedded in a densely populated matter distribution that has no clear line-of-sight to back-side reflection surfaces.

In decoupled mode, the column densities for the zeroth-order continuum and for the reflected and fluorescent line spectra may or may not be coupled to each other. If they are decoupled, they will be referred to as $N_{\text{H},z}$, and $N_{\text{H},s}$, which represent the line-of-sight column density and the global column density (in some average sense) respectively. Note that A_S should not be interpreted as a covering factor. Moreover, in a scenario in which the Compton-scattered continuum and fluorescent line flux that is observed is dominated by back-side reflection from the inner far side of the X-ray reprocessor through unobscured patches, the global covering factor cannot be constrained even in principle. The amount of “leakage” due to these patches is not related to the bulk global covering factor. In fact, the parameter A_S is more closely related (in this application) to the

fraction of the total solid angle subtended by the X-ray reprocessor that is punctured by “holes.” It should also be remembered that A_S includes the effects of any time delays between the intrinsic continuum and the response of the reflection spectra.

An alternative spectral-fitting model with a different toroidal geometry to that of the MYTORUS model, due to Brightman & Nandra (2011), is also available (see BN11). However, a detailed study by Liu & Li (2015) has shown that the BN11 toroidal model suffers from some erroneous calculations of the reprocessed X-ray continuum and line spectra, so we did not apply this model. We also note that the toroidal models of Ikeda et al. (2009) and Liu & Li (2014) are not publicly available.

3.3 The Fe $K\alpha$ Line Energy

In the BN11 and MYTORUS models, the centroid energy of the Fe $K\alpha$ line emission is not a free parameter since it is explicitly modeled as originating in neutral matter. The same is true for the Fe $K\beta$ line. In fact, in the MYTORUS model, the Fe $K\alpha$ line is explicitly modeled as the doublet $K\alpha_1$ at 6.404 keV and $K\alpha_2$ at 6.391 keV, with a branching ratio of 2:1 (see Murphy and Yaqoob (2009) for details). For Mkn 3, Shu et al. (2011) empirically measured a peak rest-frame Fe $K\alpha$ line energy of $6.396_{-0.008}^{+0.007}$ keV using high-spectral-resolution *Chandra* HEG data. However, in practice the peaks of the Fe $K\alpha$ and Fe $K\beta$ emission lines in the *Suzaku* data may be offset relative to the baseline model because of instrumental calibration systematics and/or mild ionization. The *Suzaku* data are sensitive to offsets in the Fe $K\alpha$ line peak as small as ~ 10 eV. Therefore, in the MYTORUS model we allowed the redshift parameter associated with the Fe $K\alpha$ and Fe $K\beta$ line table to vary independently of the redshift for all the other model components (which was fixed at the cosmological redshift of Mkn 3). After finding the best-fitting redshift for the line emission, the line redshift was frozen at that value before deriving statistical errors on the free parameters of the model. The BN11 spherical model does not allow the fluorescent lines to be separated from the continuum, so in that case the redshift offset had to be applied to the BN11 model continuum as well as the lines. In the tables of spectral-fitting results that we will present, the redshift offset will be given as the effective Fe $K\alpha$ line energy offset, E_{shift} , in the observed frame (or $(1+z)E_{\text{shift}}$ in the source frame, where z is the cosmological redshift). A positive shift means that the Fe $K\alpha$ line centroid energy is higher than the expected 6.400 keV.

3.4 The Fe $K\alpha$ Line Velocity Width

Using high-spectral-resolution *Chandra* HEG data, Shu et al. (2011) measured the FWHM of the Fe $K\alpha$ line in Mkn 3 to be 3140_{-660}^{+870} km s $^{-1}$. However, this is approximately half of the FWHM spectral resolution of the *Suzaku* XIS detectors at the Fe $K\alpha$ line energy, so the line is not resolved by *Suzaku*. Our approach with the *Suzaku* data is to perform the baseline spectral fits with the Fe $K\alpha$ line width fixed at a value much less than the XIS spectral resolution, at 100 km s $^{-1}$ FWHM (the same width is automatically applied to the Fe $K\beta$ line). The statistical errors on the other free parameters of the model are derived with the line width fixed at this value, but then the line width is allowed to be free in order to derive an upper limit on the FWHM.

The line broadening is achieved with the `gsmooth` convolution model in XSPEC, which convolves the intrinsic line emission spectrum with a Gaussian that has a width $\sigma(E) = \sigma_0(E/6 \text{ keV})^\alpha$, where σ_0 and α are the two parameters of the `gsmooth` model. Since the Doppler velocity width is $\Delta v \sim c(\sigma(E)/E)$, fixing $\alpha = 1$ models a velocity width that is independent of energy. The parameter σ_0 is then related to the FWHM by $\text{FWHM} \sim 2.354(c/6.0)\sigma_0 \sim 117,700\sigma_0$. Note that since the BN11 spherical model does not allow the fluorescent lines to be separated from the continuum, the `gsmooth` model in this case applies the broadening to the continuum as well as the fluorescent lines. However, the impact of the line width on the principal parameters for the continuum components, such as Γ and column densities, is negligible.

3.5 The Fe $K\alpha$ Line Flux and Equivalent Width

The Fe $K\alpha$ line flux is not explicitly an adjustable parameter because the line is produced self-consistently in both the spherical and MYTORUS models of the X-ray reprocessor. However, by isolating the emission-line table of the MYTORUS model, keeping the best-fitting model parameters, we can measure the flux of the Fe $K\alpha$ line using an energy range that excludes the Fe $K\beta$ line. The rest-frame flux is obtained by multiplying the observed flux by $(1+z)$. The equivalent width (EW) of the Fe $K\alpha$ line was calculated using the line flux and the measured (total) monochromatic continuum model flux at the observed line peak energy. The EW in the source frame was then obtained by multiplying the observed EW by $(1+z)$. Note that the Fe $K\alpha$ line flux and EW include both the zeroth-order and the Compton shoulder components of the Fe $K\alpha$ line. The Fe $K\alpha$ line is not separable from the continuum in the BN11 spherical model so we did not explicitly derive the Fe $K\alpha$ line flux and EW for this model. Note that for both the BN11 spherical model and the MYTORUS model, the Fe $K\beta$ line flux and EW are not independent of the Fe $K\alpha$ line parameters because the theoretical value of the Fe $K\beta$ to Fe $K\alpha$ branching ratio is already factored into the self-consistent Monte Carlo simulations on which the models are based (e.g. see Murphy & Yaqoob 2009).

Since the Fe $K\alpha$ line flux and EW are not explicit parameters, the statistical errors on them cannot be obtained in the

usual way. However, in the MYTORUS fits the parameter A_L can be temporarily “untied” from A_S in order to crudely estimate the statistical errors on the line flux by perturbing A_L either side of the best-fitting value.

4 PRELIMINARY SPECTRAL FITS ABOVE 2.4 KEV

Below we report the results of fitting spectral models to the *Suzaku* data above 2.4 keV. The primary purpose of these high-energy spectral fits is to explore the impact of different models on the inferred circumnuclear matter distribution in and out of the line-of-sight. More detailed spectral fitting, including additional emission lines, continuum fluxes and luminosities, and constraints on the Fe $K\alpha$ line width is deferred to §5, which describes the broadband fit.

4.1 Uniform Spherical Model Fits

In this section we give the results of applying the uniform spherical model of BN11 for the circumnuclear matter distribution in Mkn 3. See §3 and §3.1 for descriptions of the model parameters. For the sake of reproducibility, we give the exact XSPEC model expression used to set up the model:

$$\text{BN11sphere(1) model} = \text{constant} < 1 > * \text{phabs} < 2 > (\\ \text{gsmooth} < 3 > * (\text{atable}\{\text{sphere0708.fits}\} < 4 >) + \\ \text{constant} < 5 > * \text{zpowerlw} < 6 >)$$

In the above expression, we identify $\text{constant} < 1 > = C_{\text{PIN:XIS}}$, $\text{phabs} < 2 > =$ Galactic column density, and $\text{constant} < 5 > = f_s$ (associated with the distant scattering continuum). There are a total of 5 free parameters and the reduced χ^2 value for the fit is 1.732. The results are shown in Table 2 (under the column “BN11 sphere (1)”), and the best-fitting model overlaid on the unfolded spectrum is shown in Fig. 2(a). The corresponding data/model ratios are shown in Fig. 2(c). It can be seen that the fit is quite poor: the spectral curvature in the model below ~ 5 keV does not match the data, and the power-law continuum is very flat ($\Gamma = 1.292^{+0.042}_{-0.065}$), with the model continuum lying conspicuously above the data at energies higher than ~ 20 keV. In addition, the Fe abundance relative to the solar value was free in the fit and the data forced the relative Fe abundance to exceed the solar value ($X_{\text{Fe}} = 1.30^{+0.07}_{-0.06}$). The radial column density of the spherical matter distribution derived from the fit is $N_{\text{H}} = 0.498^{+0.018}_{-0.021} \times 10^{24} \text{ cm}^{-2}$ (i.e. this solution is Compton-thin).

In order to investigate whether the X-ray spectrum of Mkn 3 can be described at all in terms of an X-ray source embedded in a fully-covering shroud of material, we introduced an additional continuum component to the uniform spherical model that could compensate for its deficiencies. Namely, we added an additional power-law component that is absorbed by an additional line-of-sight absorber. We refer to the column density of the additional absorber as $N_{\text{H,Z}}$ since it is a line-of-sight quantity. A new parameter is introduced, f_{abs} , which is the fraction of the intrinsic continuum that is absorbed by the additional absorber. The photon index of the additional power-law continuum was tied to the photon index of the intrinsic continuum. The XSPEC model expression is then:

$$\text{BN11sphere(2) model} = \text{constant} < 1 > * \text{phabs} < 2 > (\\ \text{gsmooth} < 3 > * (\text{atable}\{\text{sphere0708.fits}\} < 4 >) + \\ \text{constant} < 5 > * \text{zpowerlw} < 6 > + \text{constant} < 7 > * \text{zphabs} < 8 > * \text{zpowerlw} < 9 >)$$

where $\text{constant} < 7 > = f_{\text{abs}}$, and $\text{zphabs} < 8 > = N_{\text{H,Z}}$. In this fit the Fe abundance was fixed at the solar value, so there were 6 free parameters in this model.

The spectral-fitting results are shown in Table 2 (under the column “BN11 sphere (2)”), and the best-fitting model overlaid on the unfolded spectrum is shown in Fig. 2(b). The corresponding data/model ratios are shown in Fig. 2(d). It can be seen that the fit is much improved, showing a large reduction in the $\Delta\chi^2$ of 116.2. Fig. 2(b) and Fig. 2(d) show that the continuum below ~ 5 keV, and above ~ 20 keV is now well-fitted. The power-law index of the intrinsic continuum, and the column density of the B11 spherical model are correspondingly larger ($\Gamma = 1.766^{+0.082}_{-0.071}$, $N_{\text{H}} = 1.01^{+0.44}_{-0.12} \times 10^{24} \text{ cm}^{-2}$). The additional line-of-sight column density is $N_{\text{H,Z}} = 0.143^{+0.028}_{-0.028} \times 10^{24} \text{ cm}^{-2}$, and the absorbed fraction is $f_{\text{abs}} = 0.0635^{+0.0081}_{-0.0071}$. Although this modified spherical model gives an excellent fit to the data, the additional absorbed power-law continuum is an ad hoc component and does not have an obvious physical interpretation. The spectral fitting results imply that the X-ray source is embedded in a thick, fully-covering matter distribution with a column density of $\sim 10^{24} \text{ cm}^{-2}$, yet $\sim 6\%$ of the line-of-sight is less opaque, covered by a column density that is nearly an order of magnitude smaller than the fully-covering one. A possible interpretation of this is that the X-reprocessor is clumpy, with the clumps having widely different column densities.

Table 2. Spectral-fitting results above 2.4 keV

Parameter	BN11 sphere (1)	B11 sphere (2)	MYTORUS (coupled)	MYTORUS (decoupled)
χ^2 / degrees of freedom	476.6/276	360.5/275	437.2/275	344.9/275
Free Parameters	5	6	6	6
Reduced χ^2	1.727	1.311	1.590	1.254
Null Probability	6.87×10^{-13}	4.03×10^{-4}	1.64×10^{-9}	2.65×10^{-3}
Γ	$1.292^{+0.042}_{-0.065}$	$1.766^{+0.082}_{-0.071}$	$1.503^{+0.111}_{-0.103}$	$1.664^{+0.024}_{-0.071}$
N_{H} (10^{24} cm^{-2})	$0.498^{+0.018}_{-0.021}$	$1.01^{+0.44}_{-0.12}$	$1.29^{+0.35}_{-0.35}$...
$N_{\text{H,Z}}$ (10^{24} cm^{-2})	...	$0.143^{+0.028}_{-0.028}$...	$1.000^{+0.046}_{-0.049}$
Fe abundance (ratio to solar)	$1.30^{+0.07}_{-0.06}$	1.0(f)	1.0(f)	...
$10^2 f_{\text{abs}}$ [sphere, additional absorbed fraction]	...	$6.35^{+0.81}_{-0.71}$
$N_{\text{H,S}}$ (10^{24} cm^{-2}) [MYTORUS]	$0.221^{+0.029}_{-0.021}$
θ_{obs} ($^\circ$)	$64.7^{+4.0}_{-1.7}$...
E_{shift} (eV)	$24.5^{+3.2}_{-2.8}$	$26.8^{+3.1}_{-3.1}$	$25.1^{+4.3}_{-2.8}$	$21.8^{+1.7}_{-5.4}$
A_{S} [MYTORUS]	$1.836^{+0.296}_{-0.174}$	$0.838^{+0.041}_{-0.048}$
$10^3 f_{\text{s}}$ (optically-thin scattered fraction)	$74.7^{+7.2}_{-5.3}$	$19.1^{+4.1}_{-3.5}$	$40.0^{+14.1}_{-7.4}$	$9.0^{+0.9}_{-1.0}$

Spectral-fitting results for the *Suzaku* data for Mkn 3, with a uniform spherical model of the X-ray reprocessor (BN11(1)), a uniform spherical model with an additional absorber (BN11(2)), a toroidal model with MYTORUS fitted in coupled mode, and a toroidal model with MYTORUS fitted in decoupled mode. See text for details. Fixed parameters are indicated by (f). Note that for the coupled MYTORUS model, the lower limit on Γ is not statistical, but corresponds to the smallest available value of Γ in the model tables. The best-fitting energy shifts of the Fe K α line model, E_{shift} , are given at the line peak in the observed frame, and were frozen at these values for derivation of the statistical errors on the other parameters.

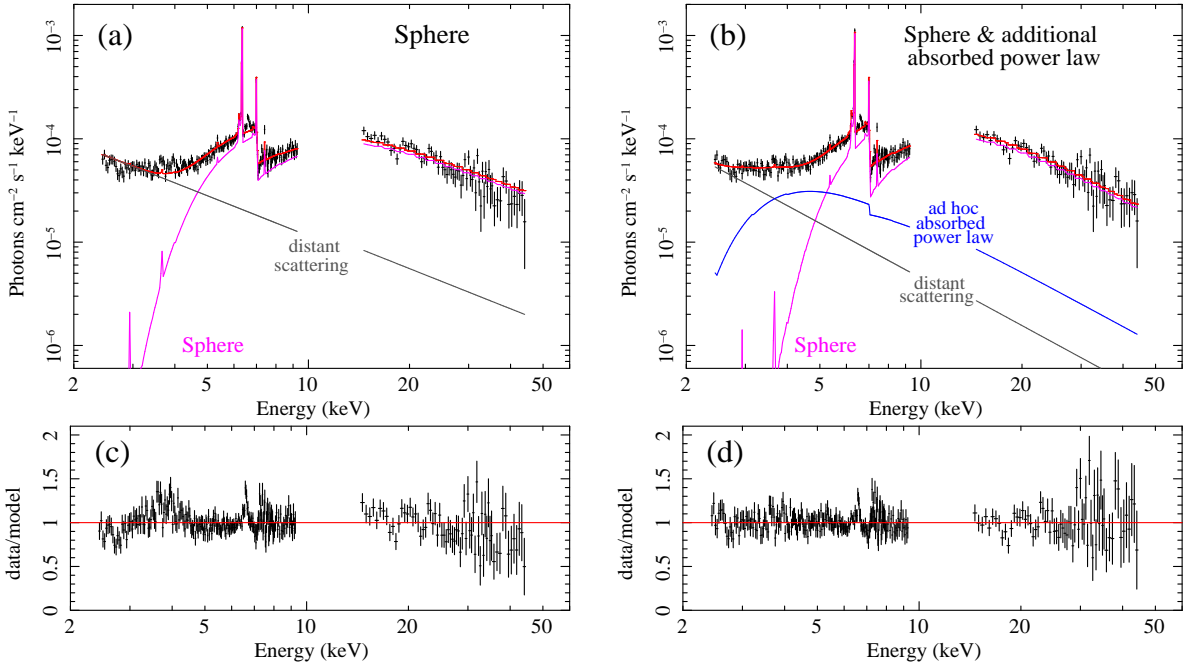


Figure 2. High-energy spectral fits to the *Suzaku* data for Mkn 3 with the uniform spherical X-ray reprocessor model (see §4.1 and Table 2). A continuum power-law component corresponding to optically-thin scattering in distant matter is included in all the fits. (a) Spherical matter distribution with no other absorption components. It can be seen that the spectral curvature in the model and data below ~ 5 keV and above ~ 25 keV are discrepant. (b) Spherical matter distribution with an additional (ad hoc) absorbed power-law component. It can be seen that the discrepancies between data and model shown in (a) are apparently resolved. (c) The data/model ratios corresponding to (a). (d) The data/model ratios corresponding to (b). (A color version of this figure is available in the online journal.)

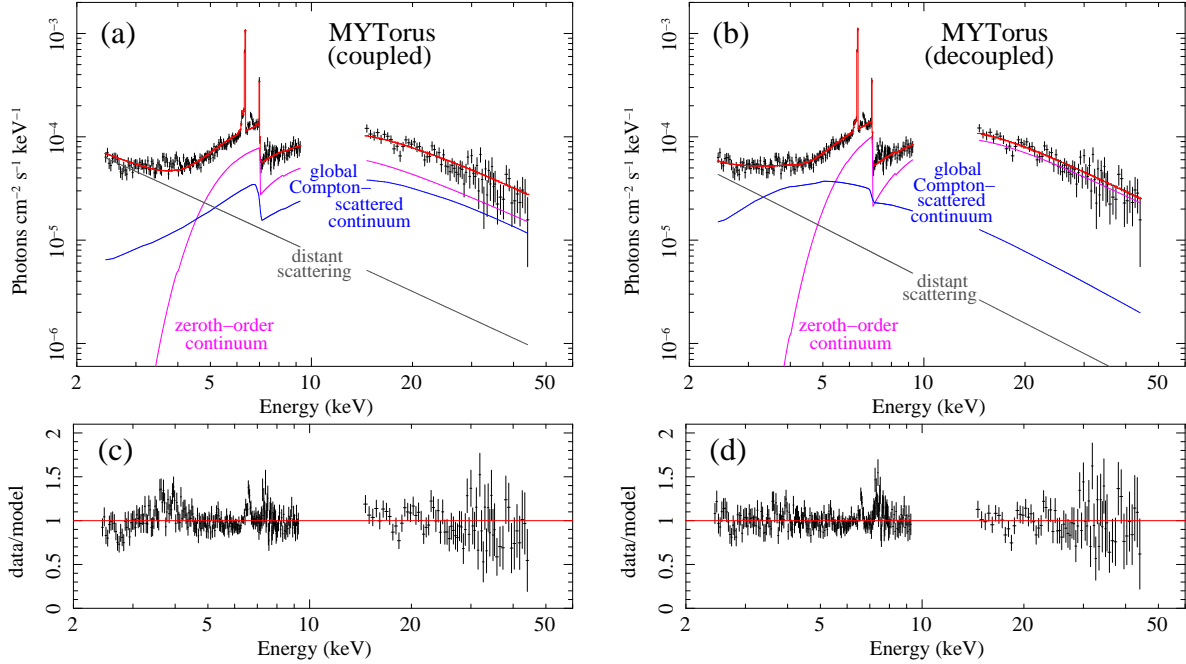


Figure 3. High-energy spectral fits to the *Suzaku* data for Mkn 3 with the MYTORUS X-ray reprocessor model (see §4.2 and Table 2). A continuum power-law component corresponding to optically-thin scattering in distant matter is included in all the fits. (a) MYTORUS model fit in coupled mode, with no other absorption components. (b) MYTORUS model fit in decoupled mode, with no other absorption components. The discrepancies between the data and spherical model shown in 2(a) are naturally resolved in this fit by the Compton-scattered continuum due to the same matter distribution that self-consistently fits the Fe $K\alpha$ emission line, requiring no additional, ad hoc, absorbed continuum component. (c) The data/model ratios corresponding to (a). (d) The data/model ratios corresponding to (b). (A color version of this figure is available in the online journal.)

4.2 MYTORUS Model Fits

In this section we give the results of fitting the Mkn 3 *Suzaku* high-energy data with the MYTORUS model, first in coupled mode, and then in decoupled mode. The XSPEC model expression is:

$$\begin{aligned} \text{MYTORUS model} = & \text{constant} < 1 > * \text{phabs} < 2 > (\\ & \text{zpowerlw} < 3 > * \text{etable}\{\text{mytorus_Ezero_v00.fits}\} < 4 > + \\ & \text{constant} < 5 > * \text{atable}\{\text{mytorus_scatteredH200_v00.fits}\} < 6 > + \\ & \text{constant} < 7 > * (\text{gsmooth} < 8 > (\text{atable}\{\text{mytl_V000010nEp000H200_v00.fits}\} < 9 >)) + \\ & \text{constant} < 10 > * \text{zpowerlw} < 11 >) \end{aligned}$$

The model parameters have been described in §3 and §3.2. Here we identify $\text{constant} < 1 > = C_{\text{PIN:xis}}$, $\text{phabs} < 2 > =$ Galactic column density, $\text{constant} < 5 > = A_S$, $\text{constant} < 7 > = A_L$, and $\text{constant} < 10 > = f_s$. In coupled mode, the column densities associated with each of the three MYTORUS model tables (components 4, 6, and 9 above) are tied together, as are the inclination angles. There are 6 free parameters in the spectral fit. The spectral-fitting results are given in Table 2, and the best-fitting model overlaid on the unfolded *Suzaku* spectrum is shown in Fig. 3(a). The corresponding data/model ratios are shown in Fig. 3(c). The fit is similar to the fit with the pure BN11 spherical model (see §4.1, Fig. 2(a), and Fig. 2(c)) in the sense that the model does not produce the correct curvature in the spectrum below ~ 5 keV, and the intrinsic power-law continuum is rather flat ($\Gamma < 1.503$; note that the lower bound in Table 2 is not statistical but corresponds to the lowest value of 1.400 in the model tables). However, the flat continuum gives an excess relative to the data above ~ 20 keV, indicating that the high-energy spectrum is steeper. The reduced χ^2 value of 1.590 is comparable to that obtained from the BN11 spherical model fit. The inclination angle and column density from the coupled MYTORUS fit are $64.7^{+4.0}_{-1.7}^\circ$ and $1.29^{+0.35}_{-0.35} \times 10^{24} \text{ cm}^{-2}$ respectively. Note that to compare this column density with that obtained from the BN11 spherical model, the MYTORUS N_H value should be multiplied by $\pi/4$, which gives the mean column density of the torus, taking into account the different incident angles of all rays from the intrinsic continuum source (see Murphy & Yaqoob 2009). The value of the constant $A_S = 1.836^{+0.296}_{-0.174}$ is nearly double the value for a time-steady intrinsic X-ray continuum illuminating a torus with a covering factor of 0.5. Thus, it is not surprising that the fit is similar to that with the fully-covering spherical model.

In Fig. 3(a) the separate contributions to the net spectrum are shown due to (1) the zeroth-order continuum (purple), (2) the Compton-scattered continuum from the thick matter out of the line-of-sight (blue), and (3) the continuum from distant scattering in the optically-thin zone (grey). It can be seen that above ~ 5 keV, the zeroth-order continuum dominates the net spectrum, whereas below ~ 5 keV, the scattered continua dominate.

Next, we fitted the data with the MYTORUS model in decoupled mode. The model expression is the same as that for the coupled mode, but now the column density for the zeroth-order continuum, $N_{\text{H,Z}}$ (associated with component 4), is independent of the global column density, $N_{\text{H,S}}$ (associated with components 6 and 9), responsible for producing the Compton-scattered continuum and the fluorescent line emission. The inclination angle of the zeroth-order continuum table becomes a dummy parameter fixed at 90° (see §3.2). The inclination angle for the Compton-scattered continuum and Fe $K\alpha$ /Fe $K\beta$ line tables is fixed at 0° , which corresponds to a scenario in which the dominant contribution to the Compton-scattered continuum and fluorescent line emission is from the back-side of material on the far side of the X-ray source, observed through “holes” in the matter distribution on the near-side to the observer. (In §5 we will investigate the effects of relaxing this assumption). The spectral-fitting results are given in Table 2, and the best-fitting model overlaid on the unfolded *Suzaku* spectrum is shown in Fig. 3(b). The corresponding data/model ratios are shown in Fig. 3(d). It can be seen that the fit is significantly better than that with the coupled MYTORUS model and it is better than both of the BN11 spherical model fits (described in §4.1). The reduced χ^2 value is 1.254, and the power-law photon index is $\Gamma = 1.664^{+0.024}_{-0.071}$. The spectral shape in the regimes that were problematic for the pure spherical model (Fig. 2(a) and Fig. 2(c)), and the coupled MYTORUS model (Fig. 3(a) and Fig. 3(c)) is very well reproduced by the decoupled MYTORUS model. Fig. 3(b) shows the separate continuum contributions to the net spectrum using the same color-coding scheme as in Fig. 3(a). From this we see that the Compton-scattered continuum in the decoupled MYTORUS model has a very similar shape to the ad hoc additional absorbed power-law component that was needed to force the spherical model to fit the data (compare the blue curves in Fig. 2(b) and Fig. 3(b)). Thus, the decoupled MYTORUS model naturally produces the continuum that is required to fit the shape of the spectrum in the $\sim 3 - 5$ keV band, and that continuum is produced by Compton scattering from *Compton-thin* material out of the line-of-sight. The column density of that material is $N_{\text{H,S}} = 0.221^{+0.029}_{-0.021} \times 10^{24} \text{ cm}^{-2}$ (the value obtained from the full-band fit described in §5 is statistically consistent with this). The column density in the line-of-sight is much larger, $N_{\text{H,Z}} = 1.000^{+0.046}_{-0.049} \times 10^{24} \text{ cm}^{-2}$. Thus, in this scenario, the departure from spherical symmetry is severe, with the implication that the global, average column density is a factor of ~ 4 smaller than that in the line-of-sight. If the circumnuclear matter is in the form of a patchy distribution of discrete clouds, with a typical column density of $N_{\text{H,S}}$, the scenario described by the decoupled MYTORUS model implies an asymmetric distribution with a larger mean number of clouds in the line-of-sight. Although the parameter A_S cannot be interpreted literally as a covering factor, the value of $A_S = 0.838^{+0.041}_{-0.048}$ (Table 2) is suggestive that a global covering factor of the order of 0.5 is not unreasonable. However, the possibility of light travel-time delays between the direct and reflected continua means that this is by no means a robust interpretation.

Note that the four sets of spectral-fitting results shown in Table 2 give different values of f_s , in the range $\sim 0.9 - 7.5\%$. It can be seen from Fig. 2 and Fig. 3 that f_s , the relative magnitude of the distant-matter power-law continuum, is controlled by how much of the data below ~ 4 keV are left unmodelled by the Compton-scattered and zeroth-order continua from the X-ray reprocessor (sphere or torus). (Above ~ 4 keV the distant-matter continuum is overwhelmed by all the other continuum components.) For example, for the pure spherical model shown in Fig. 2(a), the continua below ~ 4 keV from the X-ray reprocessor are smallest compared to the other three fits, and indeed, f_s is largest for the fit shown in Fig. 2(a) and Table 2 (column 2). At the other extreme, the decoupled MYTORUS model fit has the highest flux contribution below ~ 4 keV from the Compton-scattered and zeroth-order continua, and as can be seen from Fig. 3(b) and Table 2 (column 5), this fit also has the lowest value of f_s compared to the other three fits, as expected.

5 FULL-BAND SPECTRAL FIT WITH THE MYTORUS MODEL

5.1 Model Setup

In the previous section we presented spectral-fitting results for the Mkn 3 *Suzaku* data above 2.4 keV and showed that the decoupled MYTORUS model gave the best description of the spectrum. Although the spherical model with the addition of an ad hoc absorber gave nearly as good a fit, the additional absorber breaks the self-consistency of the model and the decoupled MYTORUS model provides a better means of modeling the implied clumpy X-ray reprocessor. The MYTORUS model also has the advantage that the line-of-sight continuum and global Compton-scattered continuum components are separable, which is especially critical if there are long-term time delays between variations in the direct and reflected continua. Here we present the spectral-fitting results for the decoupled MYTORUS model applied to the broadband *Suzaku* data (i.e. with the XIS data extended down to 0.54 keV). Including the lower energy data means that additional model components are required. Firstly, the optically-thin scattered continuum may be subject to additional absorption by matter that is extended on the scale of the galaxy, which is of course much larger than the matter distribution represented by the MYTORUS model. Thus, we added an additional uniform column density as a free parameter, which we refer to as $N_{\text{H,1}}$, that may have been too small to be

detectable in the spectral fits above 2.4 keV. We also added an optically-thin continuum emission component using the APEC model with abundances fixed at the solar values, but with the normalization and temperature of the thermal component (kT_{APEC} and A_{APEC} respectively) allowed to float in fits. This optically-thin emission component, which is commonly observed in AGN and extended on the scale of the galaxy, is also *not* absorbed by the material represented by the MYTORUS model (or at least, we observe only the portion that is unobscured by it). However, we do include an additional column density as a free parameter to allow for the possibility of absorption of the thermal component by material in addition to the primary X-ray reprocessing structure (we will refer to this column density as $N_{\text{H},2}$).

The soft X-ray spectrum of Mkn 3 is extremely complex, but the spectral resolution of the XIS is significantly worse (at all energies) than the gratings aboard *Chandra* and *XMM-Newton* ($\sim 1-2$ orders of magnitude worse than the medium-energy *Chandra* grating, depending on the energy). Previous studies of Mkn 3 using *Chandra* and *XMM-Newton* gratings have shown numerous atomic features, indicative of a predominantly photoionized spectrum originating in material with a wide range in ionization states (Sako et al. 2000; Pounds et al. 2005; Bianchi et al. 2005; Awaki et al. 2008). Thus, when grating spectra are available, CCD data cannot contribute substantially new understanding of the origin of the soft X-ray spectrum since many emission and absorption features are blended together. Nevertheless, Awaki et al. (2008) provided a detailed analysis of the same *Suzaku* X-ray spectrum of Mkn 3 as discussed in the present paper, including a comprehensive study of the atomic features found in these data. We do not repeat that analysis here and our purpose for fitting the XIS *Suzaku* soft X-ray spectrum of Mkn 3 is simply to provide an empirical parameterization of the data in order to investigate whether fitting the broadband spectrum significantly affects our conclusions about the line-of-sight and global column densities that were obtained by fitting the high-energy data with the decoupled MYTORUS model (see §4). We found that we could obtain a good parameterization of the broadband *Suzaku* spectrum by adding 11 Gaussian components to the model. Each Gaussian component is characterized by three parameters, namely the centroid energy, integrated line flux, and the energy width. In the fits, the centroid energy and flux of all 11 Gaussian components were allowed to float, with the flux allowed to become negative in order to accommodate absorption features, as opposed to emission features. We found that 10 of the Gaussian components were unresolved and the width of these was fixed at 100 km s⁻¹ FWHM. The width of the remaining Gaussian component, with centroid energy ~ 1.12 keV, was allowed to float. We note that 2 of the 11 Gaussian components model emission lines are *not* in the soft X-ray band but were small enough in EW to be omitted in the preliminary high-energy fits. These are the Fe XXV resonance line, expected at ~ 6.7 keV, and the Ni K α fluorescent line, expected at ~ 7.47 keV.

The model expression for this more complex fit with the decoupled MYTORUS model is then

$$\begin{aligned} \text{MYTORUS model} = & \text{constant} < 1 > * \text{phabs} < 2 > (\\ & \text{zpowerlw} < 3 > * \text{etable}\{\text{mytorus_Ezero_v00.fits}\} < 4 > + \\ & \text{constant} < 5 > * \text{atable}\{\text{mytorus_scatteredH200_v00.fits}\} < 6 > + \\ & \text{constant} < 7 > * (\text{gsmooth} < 8 > (\text{atable}\{\text{mytL-V000010nEp000H200_v00.fits}\} < 9 >)) + \\ & \text{constant} < 10 > * \text{zphabs} < 11 > (\text{zpowerlw} < 12 >) + \text{zphabs} < 13 > (\text{apec} < 14 >) + \\ & \sum_{i=1}^{i=11} \text{zgauss} < 14 + i >). \end{aligned}$$

There are a total of 33 free parameters, but 23 of these are associated with the Gaussian model components, and of the remaining 10, 4 parameters are determined only by the soft X-ray spectrum. Therefore only 6 free parameters affect the MYTORUS model of the X-ray reprocessor, the same number as in the high-energy fits described in §4. The best-fitting values of the model parameters and their statistical errors are shown in Table 3 and Table 4, where the latter table shows the results for the 11 Gaussian components, and the former table shows the results for the remaining model components. Fig. 4(a) shows the unfolded spectral data and model, with the corresponding data/model ratios shown in Fig. 4(b). Fig. 4(c) illustrates (in isolation of the data for greater clarity), the different continuum components that contribute to the best-fitting model. Fig. 5(a) further illustrates the broadband fit, showing the model overlaid on the counts spectrum, whilst Fig. 5(c) shows the corresponding data/model ratios. Fig. 5(b) shows a zoom on the Fe K band of the model overlaid on the counts spectrum, and Fig. 5(d) shows the corresponding data/model ratios. The reduced χ^2 value is 1.069, and it can be seen from Fig. 5 that the fit is excellent.

5.2 X-ray Reprocessor Column Densities

The line-of-sight column density from the MYTORUS model, $N_{\text{H},Z}$, is $0.902^{+0.012}_{-0.013} \times 10^{24}$ cm⁻², and the global column density out of the line-of-sight, $N_{\text{H},S}$, is $0.234^{+0.012}_{-0.010} \times 10^{24}$ cm⁻² (see Table 3). These column densities are entirely consistent with the corresponding values obtained from the decoupled MYTORUS model fitted to the data above 2.4 keV (Table 2). The value of A_S in Table 3 is $1.128^{+0.041}_{-0.038}$, or $\sim 35\%$ higher than the value obtained from the high-energy fits. However, it can be

Table 3. Results of fitting *Suzaku* data for Mkn 3 with the MYTORUS model

Parameter	Value
χ^2	300.3
degrees of freedom	281
Free parameters (Gaussian components)	23
Free parameters (MYTORUS, other continua)	10
Reduced χ^2	1.069
Null probability	0.206
Γ	$1.473^{+0.007}_{-0.009}$
$N_{\text{H,Z}}$ (10^{24} cm $^{-2}$)	$0.902^{+0.012}_{-0.013}$
$N_{\text{H,S}}$ (10^{24} cm $^{-2}$)	$0.234^{+0.012}_{-0.010}$
A_S	$1.128^{+0.041}_{-0.030}$
$10^3 f_s$ (optically-thin scattered fraction)	$17.6^{+0.8}_{-0.7}$
$N_{\text{H,1}}$ (10^{22} cm $^{-2}$)	$0.221^{+0.039}_{-0.022}$
kT_{APEC} (keV)	$0.751^{+0.016}_{-0.008}$
A_{APEC} (10^{-3} photons cm $^{-2}$ s $^{-1}$ keV $^{-1}$)	$1.856^{+0.035}_{-0.053}$
$N_{\text{H,2}}$ (10^{22} cm $^{-2}$)	$0.060^{+0.012}_{-0.008}$
E_{shift} (eV)	$18.7^{+3.0}_{-3.1}$
$I_{\text{Fe K}\alpha}$ (10^{-5} photons cm $^{-2}$ s $^{-1}$)	$5.07^{+0.20}_{-0.18}$
$\text{EW}_{\text{Fe K}\alpha}$ (eV)	470^{+18}_{-17}
Fe K α FWHM (km s $^{-1}$)	100 (f) (< 3060)
$F_{\text{obs}}[0.5-2 \text{ keV}]$ (10^{-12} erg cm $^{-2}$ s $^{-1}$)	0.64
$F_{\text{obs}}[2-10 \text{ keV}]$ (10^{-12} erg cm $^{-2}$ s $^{-1}$)	6.64
$F_{\text{obs}}[10-30 \text{ keV}]$ (10^{-12} erg cm $^{-2}$ s $^{-1}$)	39.8
$L_{\text{obs}}[0.5-2 \text{ keV}]$ (10^{43} erg s $^{-1}$)	0.26
$L_{\text{obs}}[2-10 \text{ keV}]$ (10^{43} erg s $^{-1}$)	2.64
$L_{\text{obs}}[10-30 \text{ keV}]$ (10^{43} erg s $^{-1}$)	16.0
$L_{\text{intr}}[0.5-2 \text{ keV}]$ (10^{43} erg s $^{-1}$)	2.00
$L_{\text{intr}}[2-10 \text{ keV}]$ (10^{43} erg s $^{-1}$)	2.47
$L_{\text{intr}}[10-30 \text{ keV}]$ (10^{43} erg s $^{-1}$)	17.8
$L_{\text{APEC}}[0.2-10 \text{ keV}]$ (10^{41} erg s $^{-1}$)	2.0

Spectral-fitting results for Mkn 3 including low-energy data, described in §5. The results for the Gaussian line components for the same fit are shown in Table 4. The best-fitting energy shift of the Fe K α line model, E_{shift} , is given at the line peak in the observed frame, and was frozen at that value for derivation of the statistical errors for other model parameters. The Fe K α line is unresolved and its width was fixed at 100 km s $^{-1}$ FWHM, but allowed to float for deriving the upper limit. The observed fluxes, F_{obs} , are total fluxes in the stated energy bands in the observed frame. The observed and intrinsic luminosities, L_{obs} and L_{intr} respectively, are total luminosities in the stated energy band in the source rest frame. All other model parameters are in the source rest frame. The intrinsic luminosities are those for the incident continuum, with all absorption and reflection turned off. Some model extrapolation was employed for fluxes and luminosities for energy intervals with no data coverage.

seen, by comparing the spectral decomposition for the two fits in Fig. 3(b) and Fig. 4(a), that the absolute flux level of the Compton-scattered continuum is essentially the same for the two fits. Since A_S is a parameter that controls the flux level of the Compton-scattered continuum *relative* to the intrinsic continuum, the absolute flux of the Compton-scattered continuum is controlled by the product of the normalization of the intrinsic continuum and A_S . We see from Table 2 and Table 3 that the photon index, Γ , of the intrinsic continuum for the broadband fit is significantly flatter than that for the high-energy fit, and the normalization at 1 keV of the intrinsic continuum for the broadband fit is consequently lower than that for the high-energy fit. Thus, a higher value of A_S is required in the broadband fit to maintain the same absolute flux level of the Compton-scattered continuum, and the different values of A_S have an insignificant impact on the inferred global column densities. The reason for the flatter intrinsic continuum for the broadband fit will be discussed below, in §5.4.

It is important to note that all of the column densities out of the line-of-sight that we have obtained for the X-ray reprocessor are *Compton-thin*, for both the BN11 spherical model and the MYTORUS model. (Recall that for the coupled MYTORUS model, the equatorial column density obtained from the fit must be multiplied by $(\pi/4)$ to obtain the mean column density averaged over incident angles.) Moreover, the values of the line-of-sight column density obtained from the various fits are either only just, or nearly Compton-thick. In the broadband fit with the decoupled MYTORUS model, the global mean column density in Mkn 3 is a long way (a factor of ~ 5) from being Compton-thick. Reflection from Compton-thin matter has a different spectral shape to that from a disc with infinite column density that is commonly used to model AGN spectra. Fig. 4 shows that the Compton-thin reflection component that we infer in from the MYTORUS broadband fit for Mkn 3 (blue curves) is not negligible, and in fact dominates the spectrum in the $\sim 3 - 5$ keV band, it being larger than both the zeroth-order

Table 4. Additional Gaussian components included in the MYTORUS model fit to the *Suzaku* data

Line	Energy (keV)	Flux (10^{-5} photons cm^{-2} s^{-1})	EW (eV)	$\Delta\chi^2$	Likely ID
1	$0.580^{+0.004}_{-0.004}$	$8.54^{+0.78}_{-1.31}$	949^{+87}_{-146}	184.0	O VII He-like triplet
2	$0.674^{+0.005}_{-0.004}$	$3.85^{+0.53}_{-0.40}$	321^{+44}_{-33}	151.9	O VIII Ly α
3	$0.748^{+0.007}_{-0.005}$	$2.75^{+0.29}_{-0.46}$	$32.7^{+3.5}_{-5.5}$	79.8	O VII RRC
4	$0.923^{+0.006}_{-0.007}$	$1.64^{+0.24}_{-0.28}$	$26.0^{+3.8}_{-4.4}$	196.1	Ne IX He-line triplet
5	$0.976^{+0.008}_{-0.007}$	$-1.06^{+0.19}_{-0.20}$	$-18.3^{+3.3}_{-3.5}$	116.5	Ne X Ly α
6	$1.057^{+0.006}_{-0.006}$	$1.14^{+0.15}_{-0.18}$	$51.8^{+6.8}_{-8.2}$	132.8	Fe XXII L
7	$1.118^{+0.081}_{-0.049}$	$1.00^{+0.15}_{-0.19}$	$45.5^{+6.8}_{-8.6}$	89.1	Fe XXIII L
8	$1.268^{+0.027}_{-0.025}$	$0.15^{+0.11}_{-0.10}$	$8.3^{+6.1}_{-5.6}$	86.9	Ne X Ly β /Mg K α
9	$1.359^{+0.008}_{-0.009}$	$0.55^{+0.12}_{-0.09}$	$36.7^{+8.0}_{-6.0}$	23.0	Mg XI He-like triplet
10	$6.699^{+0.018}_{-0.019}$	$0.70^{+0.13}_{-0.13}$	$58.3^{+10.8}_{-10.8}$	96.7	Fe XXV(r)
11	$7.442^{+0.056}_{-0.050}$	$0.32^{+0.12}_{-0.11}$	$53.3^{+20.0}_{-18.3}$	6.1	Ni K α

The best-fitting parameters and statistical errors of the Gaussian model components that are part of the model results shown in Table 3 and described in §5. A negative flux indicates an absorption feature. All except Gaussian component number 7 are unresolved: the width of each unresolved component was fixed at 100 km s $^{-1}$ FWHM. The width for component number 7 was a free parameter, yielding a width of $33,290^{+11,700}_{-6,540}$ km s $^{-1}$ FWHM (likely due to a blend of two or more features). The $\Delta\chi^2$ values for each line correspond to the change in χ^2 obtained when that line was removed from the model. The likely line ID’s are shown, within the systematic uncertainties in the energy scale. See Awaki et al. (2008) for a more detailed description of the *Suzaku* soft X-ray line spectrum, along with theoretical expected values of line centroid energies.

(line-of-sight) absorbed continuum and the continuum from distant scattering. It is principally the Fe K α emission line and the continuum curvature below ~ 6 keV that constrains this Compton-thin reflection continuum. The excellent quality of the fit in the Fe K band shown in Fig. 5(c) and Fig. 5(d) is particularly noteworthy, considering that the Fe K α line, Fe K β line, and Fe K edge are all determined self-consistently relative to the reflection continuum so they were not allowed to change independently of the reflection continuum. (Note that the parameter A_S varies the reflection continuum and Fe K α and Fe K β lines *all together* and does not allow the continuum and lines to be independent.) In order to further illustrate the statistical significance of the result that the line-of-sight and global column densities in Mkn 3 obtained from the decoupled MYTORUS fit are very different, in Fig. 6 we show the joint, two-parameter 68%, 90%, and 99% confidence contours of $N_{\text{H,S}}$ versus $N_{\text{H,Z}}$. It can be seen that the constraints on both column densities are robust even at the 99% confidence level.

In a clumpy medium the Compton-scattered reflection continuum from individual clumps can take on a variety of shapes, depending on the average column density of the clump, the direction of the observer’s line-of-sight relative to the direction of the illuminating intrinsic continuum, and the obscuration by other clumps. The shape of the reflection continuum will lie between the two extreme cases corresponding to the Compton-scattered photons being observed from the same or opposite side of the clump relative to the illuminating continuum (e.g. see Yaqoob 2012, Liu & Lu 2014). Considering the entire clumpy matter distribution, the first of the two extremes could correspond to a situation in which the reflection continuum is dominated by the reflection continuum from the back-side illumination of clumps on the opposite side of the X-ray source, relative to the observer, reaching the observer through unblocked patches, or “holes,” in the near-side of the matter distribution. The other extreme could correspond to the reflection continuum being dominated by Compton-scattered photons escaping from the near-side of the matter distribution, from surfaces that are on the sides opposite to the illuminated surfaces. The latter scenario can be thought of as “transmitted reflection.” In the optically-thin limit that Compton-scattered photons experience only one scattering and no further interaction with the clumpy matter distribution, the two extreme cases described above will result in reflection spectra that are indistinguishable. Thus, as the column density of the distribution is varied from being Compton-thick to Compton-thin, the reflection continuum shape will depend less and less on the detailed geometrical distribution, filling factor, and size of the clumps. Using the MYTORUS model we can approximately mimic the two extremes described above with a face-on inclination angle and an edge-on inclination angle, corresponding to clumps observed predominantly by back-side reflection and “transmitted reflection” respectively (see Fig. 6 in Yaqoob 2012, and the associated discussion).

In the decoupled MYTORUS fit to the broadband Mkn 3 data described earlier (see Table 3), the inclination angle of the torus was set to face-on, corresponding to one of the two extremes outlined above. From this, we found a column density that is Compton-thin, $N_{\text{H,S}} = 0.234^{+0.012}_{-0.010} \times 10^{24}$ cm $^{-2}$. Therefore, in light of the earlier discussion, if we set the torus inclination angle to edge-on, we should expect to obtain a similar column density (but note that Compton-thin does not equate with optically-thin since the optical depth is energy-dependent). We performed such a fit (torus inclination angle set to 90 $^\circ$) and indeed obtained a similar column density, $N_{\text{H,S}} = 0.210^{+0.012}_{-0.008} \times 10^{24}$ cm $^{-2}$. The fit was not as good as the face-on case but still acceptable ($\chi^2 = 342.5$, for 281 degrees of freedom, the same number as for the face-on case). We obtained a line-of-sight

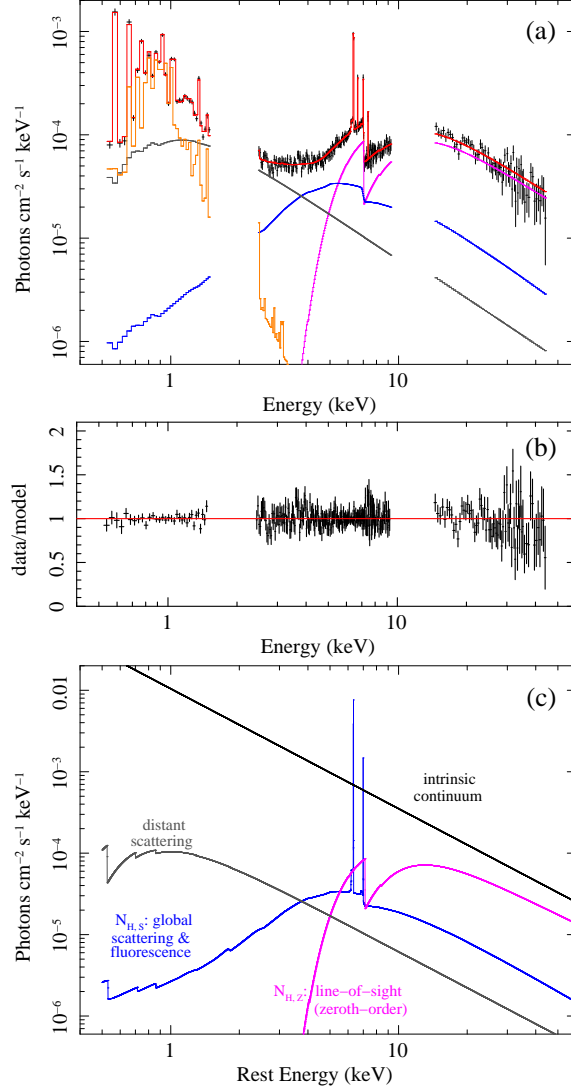


Figure 4. (a) Full, broadband spectral fit to the *Suzaku* Mkn 3 data with the best-fitting MYTORUS model (see §5, Table 3, and Table 4), showing the unfolded spectrum, the net model spectrum, and the individual model components. Note that some emission-line features appear to be artificially narrower than they are in an unfolded spectrum. See Fig. 5 showing the same fit overlaid on the counts spectrum, which does not suffer from this effect. (b) Data/model ratios corresponding to (a), the intrinsic continuum, and the optically-thin scattered component from distant matter. Not shown in is the soft X-ray extended optically-thin thermal emission shown in brown in (a). (A color version of this figure is available in the online journal.)

column density of $N_{\text{H},Z} = 0.997^{+0.023}_{-0.011} \times 10^{24} \text{ cm}^{-2}$, or $\sim 10\%$ higher than the face-on case. The value of A_s was $1.55^{+0.06}_{-0.04}$, or $\sim 40\%$ higher than the face-on case. The higher value is a result of the edge-on “transmitted reflection” spectrum being more suppressed relative to the intrinsic continuum than the back-side reflection spectrum for the face-on case. We conclude that the average global column density of the X-ray reprocessor in Mkn 3 inferred from the MYTORUS fits is Compton-thin and of the order of $\sim 0.2 - 0.25 \times 10^{24} \text{ cm}^{-2}$ regardless of the detailed geometry and orientation of the reprocessor.

5.3 Fe $K\alpha$, Fe $K\beta$ Emission Lines, and Fe K Edge

Table 3 shows that the Fe $K\alpha$ line flux and EW were measured to be $5.07^{+0.20}_{-0.18} \times 10^{-5} \text{ photons cm}^{-2} \text{ s}^{-1}$, and $470^{+17}_{-18} \text{ eV}$ respectively, where the EW was calculated with respect to the total continuum at the line peak (in the AGN frame). The Fe $K\alpha$ line is unresolved with the XIS, and the upper limit obtained on the line width ($\text{FWHM} < 3060 \text{ km s}^{-1}$) is consistent with the *Chandra* HEG measurement of $3140^{+870}_{-660} \text{ km s}^{-1}$ reported in Shu et al. (2011). Using the simple prescription of Netzer (1990) for relating the virialized velocity of matter orbiting a black hole, the characteristic radius of the line-emitting region can be written $r \sim (4/3)(c/\text{FWHM})^2 r_g$, where $r_g \equiv GM/c^2$ is the gravitational radius. For Mkn 3, the *Chandra* HEG Fe $K\alpha$ line FWHM corresponds to $r \sim 1.22 \times 10^4 r_g$, or for a black-hole mass of $4.5 \times 10^8 M_\odot$ (Woo & Urry 2002), $r \sim 0.27 \text{ pc}$. For

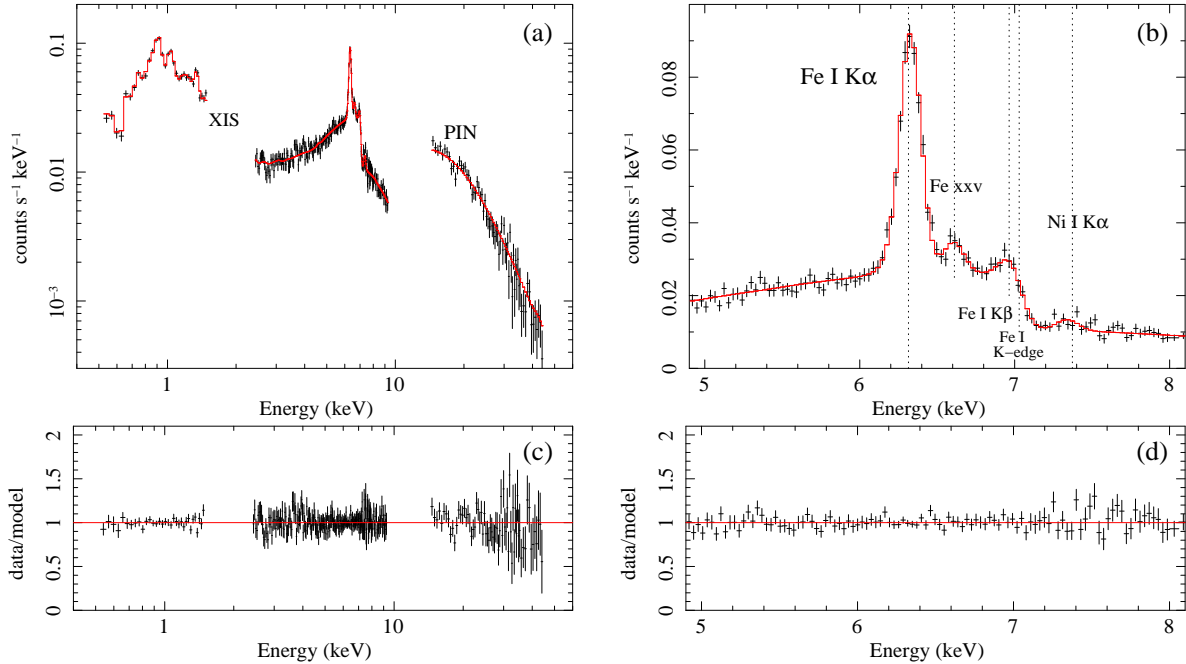


Figure 5. Same broadband spectral fit as in Fig. 4 (see §5, Table 3, and Table 4), this time showing the decoupled MYTORUS model overlaid on the *Suzaku* counts spectra for Mkn 3. (a) The full broadband XIS and PIN data (black) overlaid with the best-fitting MYTORUS model (red). Note that the energy range in the 1.5–2.4 keV band is omitted due to calibration uncertainties (see text for details). (b) The data and model shown in (a), zoomed in on the Fe K region, showing the detailed fit to the Fe K α emission line and other atomic features as labeled. Note that the flux of the model Fe K α line is not controlled by an arbitrary parameter but calculated self-consistently from the same matter distribution that produces the global Compton-scattered continuum (see Fig. 4). The dotted lines correspond to the expected energies of the labeled atomic features in the observed frame. The data to model ratios corresponding to (a) and (b) are shown in (c) and (d) respectively. (A color version of this figure is available in the online journal.)

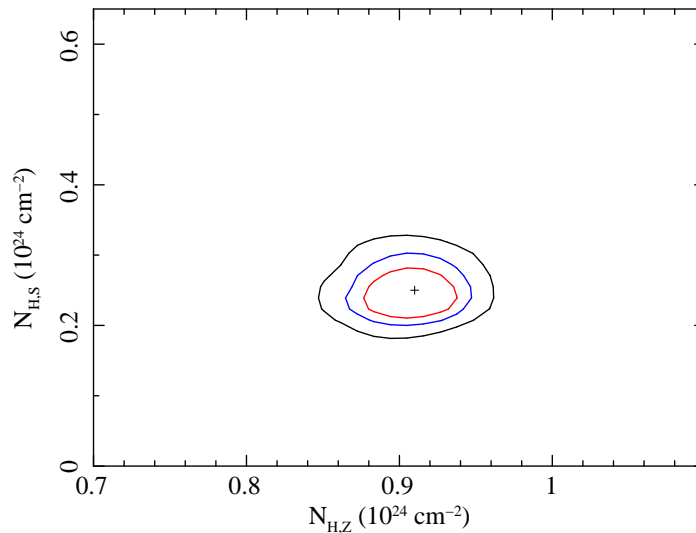


Figure 6. Two-parameter confidence contours of the global column density, $N_{\text{H,S}}$, versus the line-of-sight column density, $N_{\text{H,Z}}$, obtained from fitting the MYTORUS model to the Mkn 3 broadband *Suzaku* data (see §5, Table 3, and Table 4). The black, blue, and red contours correspond to 99%, 90%, and 68% confidence respectively. (A color version of this figure is available in the online journal.)

the *Suzaku* upper limit measurement of the FWHM, which is approximately equal to the *Chandra* HEG best-fit value, the preceding values of r are upper limits.

The MYTORUS model self-consistently calculates the Compton shoulder of both the Fe K α and Fe K β lines, but the ratio of the flux in the Compton shoulder to that in the core of the Fe K α line for the small global column density in the best-fitting broadband model is only $\sim 9\%$ (see Yaqoob & Murphy 2010). The MYTORUS model also self-consistently calculates the flux and profile of the Fe K β line. It can be seen from the model overlaid on the data in the Fe K region in Fig. 5(b), and the

corresponding remarkably flat residuals in Fig. 5(d), that the fit to the Fe K α line, the Fe K β line, and the Fe K edge is excellent, despite the fact that no empirical adjustments were applied to either of the Fe fluorescent lines relative to the Compton-scattered continuum, and the Fe abundance was fixed at the solar value. For a given set of model parameters that determine the Compton-scattered continuum, the Fe fluorescent lines are completely determined. In the decoupled MYTORUS model solution, the spectrum at the Fe K edge is dominated by the line-of-sight extinction and not the Compton-reflection continuum.

We note that previous results for the Compton shoulder in Mkn 3 were based on fitting the shoulder with nonphysical, ad hoc models, independent of the flux of the Fe K α line core. Awaki et al. (2008) claimed a detection of the Compton shoulder in the same *Suzaku* data for Mkn 3 as modeled in the present paper. They used a rectangular shape for the shoulder, with a width of 156 eV, and found a ratio of flux in the shoulder to that of the line core of $10 \pm 8\%$ (one-parameter error). The peak energy of the line core increased by 6 eV when the Compton shoulder was included. However, they did not give a statistical significance for the detection of the shoulder, but it can be seen from the confidence contours of line core peak energy versus Compton shoulder to line core flux ratios in Fig. 5 of Awaki et al. (2008), that the flux of the shoulder is consistent with zero at 90% confidence for two parameters. Pounds et al. (2005), using *XMM-Newton* data for Mkn 3, forced a Compton shoulder in the fit, which forced the line core centroid energy to increase above the value for neutral Fe, to 6.43 ± 0.01 keV. Despite reporting a ratio of the Compton shoulder to line core flux of $\sim 20\%$ (with no statistical errors given), Pounds et al. (2005) stated that inclusion of the shoulder did not result in a statistical improvement of the fit. We note that the expected ratio of the flux in the Compton shoulder to that in the line core from Compton-thick matter is $\sim 25 - 30\%$, depending on the geometry and orientation of the line-emitting structure (e.g. see George & Fabian 1991; Matt 2002; Yaqoob & Murphy 2010). Our best description of the *Suzaku* data with the MYTORUS model indicates that the matter distribution is globally Compton-thin, so the ratio of the flux in the Compton shoulder to that in the line core is not expected to be as high as that for an origin of the Fe K α line in Compton-thick matter. However, even if the Fe K α line were formed in Compton-thick matter, it has been shown in Yaqoob & Murphy (2010) that if the velocity broadening of the Fe K α line, or the detector spectral resolution, is larger than ~ 2000 km s $^{-1}$ FWHM, the Compton shoulder will be rendered too smeared to be detectable, even in principle.

5.4 Continua, Fluxes, and Luminosities

Table 3 shows that the photon index of the intrinsic power-law continuum for the broadband decoupled MYTORUS fit is $\Gamma = 1.473_{-0.009}^{+0.007}$, which is rather flat. The high-energy fit with the same model gave $\Gamma = 1.664_{-0.071}^{+0.024}$ (Table 2, column 5). Amongst the high-energy fits described in §4, only the pure spherical model gave an intrinsic continuum flatter than this (Table 2, column 3). The reason for the flatter intrinsic continuum in the broadband fit is that the steep rise in the observed spectrum below ~ 2 keV (see Fig. 4) is accommodated by the thermal continuum emission (APEC model component) and this forces the intrinsic continuum at low energies to be pushed down in flux. Without the soft thermal component, a single, steeper power-law continuum cannot simultaneously accommodate the soft low-energy spectrum and the hard high-energy spectrum. Although statistical studies have shown that the average intrinsic photon index is characteristically $\Gamma \sim 1.8$ for both type 1 and type 2 AGN (e.g. Dadina 2007, 2008, and references therein), those results do show a range in Γ of 1.5–2.5, with a non-negligible number of outliers even outside this range. However, it must be borne in mind that distributions of Γ in previous studies were obtained from fitting the ad hoc models invoking disc reflection with infinite column density, and unphysical exponential cutoffs applied to the high-energy intrinsic continua. Studies of the distribution of the intrinsic power-law continuum photon index need to be revisited, applying the new models of finite column density X-ray reprocessors, such as described in the present paper, to large samples of AGN. Results for high statistical quality data for individual sources and small samples are now beginning to emerge (e.g. see Brightman et al. 2015 and references therein), but further work is required to establish robust parameter distributions.

From Table 3 it can be seen that the fraction of the intrinsic power-law continuum required to produce the optically-thin, distant-matter scattered continuum is $f_s = 0.0176_{-0.0007}^{+0.0008}$, which is within the range generally observed in Seyfert 2 galaxies (e.g. Turner et al. 1997). The value of f_s obtained from the broadband decoupled MYTORUS fit is nearly a factor of 2 larger than the corresponding value obtained from the decoupled MYTORUS high-energy fit ($0.0090_{-0.0010}^{+0.0009}$, see Table 2). However, if we compare the spectral decomposition for the high-energy and broadband decoupled MYTORUS fits shown in Fig. 3(b) and Fig. 4(a) respectively, we see that the absolute flux of the distant-matter scattered continuum is essentially the same in both cases. Since f_s is a parameter that controls the flux level of the distant-matter power-law continuum *relative* to the intrinsic continuum, the absolute flux of the distant-matter continuum is controlled by the product of the normalization of the intrinsic continuum and f_s . The situation is very similar to that of the parameter A_S being different for the broadband and high-energy fits, and as we discussed earlier, the photon index, Γ , of the intrinsic continuum for the broadband fit is significantly flatter than that for the high-energy fit. Consequently, the normalization of the intrinsic continuum at 1 keV for the broadband fit is lower than that for the high-energy fit. Thus, a higher value of f_s is required in the broadband fit to maintain the same absolute flux level of the distant-matter continuum. The reason for the flatter intrinsic continuum for the broadband fit has

already been discussed earlier. The column density associated with the optically-thin, distant-matter scattered continuum is $N_{\text{H},1} = 0.221^{+0.039}_{-0.022} \times 10^{22} \text{ cm}^{-2}$.

Continuum fluxes and luminosities obtained from the broadband decoupled MYTORUS model fit are shown in Table 3, in three energy bands: 0.5–2 keV, 2–10 keV, and 10–30 keV. For fluxes, these energy bands are in the observed frame, but for luminosities, the lower and upper energies in each band are quantities in the source frame, so that they appear redshifted in the observed frame. For regions where there were no data, the model was extrapolated. The 0.5–2 keV, 2–10 keV, and 10–30 keV fluxes are 0.64, 6.64, and $39.8 \times 10^{-12} \text{ erg cm}^{-2} \text{ s}^{-1}$ respectively. These values are roughly in the mid-range of historical flux levels of Mkn 3 (e.g. Iwasawa et al. 1994; Guainazzi et al. 2012).

In Table 3, observed luminosities are denoted by L_{obs} (derived directly from the best-fitting model), and intrinsic luminosities are denoted by L_{intr} (derived from only the best-fitting intrinsic power-law continuum). The 0.5–2 keV, 2–10 keV, and 10–30 keV values for L_{obs} we obtained are 0.26, 2.64, and $16.0 \times 10^{43} \text{ erg s}^{-1}$ respectively. The intrinsic luminosities that we obtained in the 0.5–2 keV, 2–10 keV, and 10–30 keV bands are 2.00, 2.47, and $17.8 \times 10^{43} \text{ erg s}^{-1}$ respectively. These luminosities are sensitive to the value of Γ , which complicates comparison with the corresponding luminosities in the literature that were obtained using the ad hoc models, which yield different values of Γ . Also, since the ad hoc models have an adjustable parameter for the Compton-thick reflection continuum amplitude, a model that is globally Compton-thin will not necessarily yield an intrinsic luminosity that is smaller than previous analyses that assumed Compton-thick reflection. In fact, using the same *Suzaku* data as in the present study, Awaki et al. (2008) obtained a 2–10 keV intrinsic luminosity of $\sim 1.7 \times 10^{43} \text{ erg s}^{-1}$, which is actually lower than the value of $\sim 2.6 \times 10^{43} \text{ erg s}^{-1}$ that we obtained from the broadband MYTORUS fit. The difference can be attributed largely to the smaller value of Γ that we obtained from broadband MYTORUS fit. This can easily be demonstrated by calculating the luminosity of the intrinsic power law with $\Gamma = 1.8$ (closer to the value obtained by Awaki et al. 2008), but with same normalization of the intrinsic power law as in the broadband MYTORUS fit. The result is a 2–10 keV luminosity that is similar to the Awaki et al. (2008) value.

Table 3 shows that the temperature obtained for the optically-thin thermal continuum from the APEC model is $kT_{\text{APEC}} = 0.751^{+0.016}_{-0.008} \text{ keV}$, typical of Seyfert 2 galaxies (e.g. Turner et al. 1997). The column density associated with the optically-thin thermal continuum is $N_{\text{H},2} = 0.060^{+0.012}_{-0.008} \times 10^{22} \text{ cm}^{-2}$. Table 3 also shows that the intrinsic luminosity of the best-fitting APEC model alone (in the 0.2–10 keV band) is $L_{\text{APEC}} = 2.0 \times 10^{41} \text{ erg s}^{-1}$. This is less than 0.04% of the bolometric luminosity of Mkn 3, which is estimated to be $\sim 5 - 6 \times 10^{44} \text{ erg s}^{-1}$ by Vasudevan et al. (2010). This would appear to align with the conclusion of Brandl et al. (2006, 2007) that Mkn 3 is AGN-dominated as opposed to starburst-dominated, based on a study of mid-infrared flux ratios.

5.5 Gaussian Model Components

Table 4 shows the results for the 11 Gaussian model components that were included in the broadband decoupled MYTORUS fit. Shown are the centroid energies, fluxes, equivalent widths, and a $\Delta\chi^2$ value for each line. The latter corresponds to the increase in χ^2 when the associated line is removed, and the model re-fitted. This gives some indication of the statistical significance of each line component. In this context, we note that a value of $\Delta\chi^2$ of 11.83 corresponds to a confidence level of 3σ for two interesting parameters. The $\Delta\chi^2$ values (see Table 4) are much larger than this for all of the lines except for line number 11, for which $\Delta\chi^2 = 6.1$, indicating a confidence level of $\sim 95\%$.

The velocity width of all except one of the Gaussian model components was fixed at 100 km s^{-1} FWHM, a value much less than the instrument resolution. For the component that the line width was free (line number 7), we obtained $33,290^{+11,700}_{-6,540} \text{ km s}^{-1}$ FWHM. However, as stated earlier, due to the limited spectral resolution of CCD detectors, some of the Gaussian model components may be blends of two or more features, or even artifacts of incorrect modeling of the soft X-ray spectrum. Our intention is not to attempt a detailed analysis of the soft X-ray spectrum since this has already been done with higher spectral resolution instruments (Sako et al. 2000; Pounds et al. 2005; Bianchi et al. 2005), and it has also been done for these same *Suzaku* data by Awaki et al. (2008).

The Gaussian component number 5 in Table 4 has a negative flux and represents an absorption line at a rest-frame energy of $0.976^{+0.008}_{-0.007} \text{ keV}$. Although the energy of the line is approximately that expected for Ne X resonance absorption (1.022 keV^6), we note that such an absorption feature has never previously been reported for Mkn 3. In fact, previous studies of Mkn 3 with *Chandra* grating data (Sako et al. 2000), *XMM-Newton* grating data (Pounds et al. 2005; Bianchi et al. 2005), and the *Suzaku* data in the present study (Awaki et al. 2008), have not reported the detection of any absorption lines at all, only emission lines. It is very likely that the absorption line reported in Table 4 in the present study is an artifact of our overly simplistic modeling. In particular the combination of the optically-thin thermal continuum, in conjunction with other continuum components, could conspire to produce an artificial absorption trough. We note that the model used by Awaki et al. (2008) for the same *Suzaku* data as in the present study, did not include an optically-thin thermal model component, but

⁶ <http://www.pa.uky.edu/peter/atomic>

only Gaussian model components. Also, the observed energy of the line, $0.976_{-0.007}^{+0.008}$ keV, compared to the expected 1.022 keV would imply a redshift, yet such photoionized gas in AGN is characteristically observed in outflow (e.g. Laha et al. 2014, and references therein).

It can be seen from Table 4 that the Ni $K\alpha$ fluorescent line energy measured from the *Suzaku* data, namely $7.442_{-0.050}^{+0.056}$ keV, is consistent with the theoretical value of 7.472 keV (e.g., Bearden 1967). The EW of the Ni $K\alpha$ line is $\sim 58_{-18}^{+20}$ eV, a factor of ~ 2 larger than the calculated Monte Carlo value appropriate for the decoupled MYTORUS fit (see Yaqoob & Murphy 2011b), suggestive of an overabundance of Ni relative to the Anders and Grevesse (1989) solar value.

6 SUMMARY

We have revisited the *Suzaku* X-ray spectrum of the Seyfert 2 galaxy Mkn 3 to investigate the distribution of circumnuclear matter (the X-ray reprocessor), using models that self-consistently account for the “neutral,” narrow, Fe $K\alpha$ emission line, and Compton reflection of the continuum and line emission. Our methodology is able to disentangle the column density in the line-of-sight from the global average column density. Our conclusions are summarized below.

(i) We tested the data against a uniform spherical distribution using the model of Brightman and Nandra (2011), and obtained a radial column density of $\sim 0.50 \pm 0.02 \times 10^{24}$ cm $^{-2}$. However, the fit was very poor and the model could not produce the correct continuum shape whilst simultaneously accounting for the Fe $K\alpha$ line, even when we allowed the Fe abundance to be a free parameter. The fit can be improved by adding additional continuum components and absorbers but the model is then no longer that of a uniform, spherically symmetric distribution.

(ii) Applying the MYTORUS model of Murphy and Yaqoob (2009) in “coupled mode,” yielded an equatorial column density of $\sim 1.29 \pm 0.35 \times 10^{24}$ cm $^{-2}$ and an inclination angle of $64.7_{-1.7}^{+4.0}$ ° for the toroidal structure, but again, the fit was not satisfactory, due to the lack of a self-consistent solution for the continuum and Fe $K\alpha$ line.

(iii) Applying the MYTORUS model in “decoupled mode,” gave an excellent fit, and the best description of the data, yielding a global column density, $N_{H,S}$, of $\sim 0.234_{-0.010}^{+0.012} \times 10^{24}$ cm $^{-2}$ that is very different to the line-of-sight column density, $N_{H,Z}$, of $0.902_{-0.013}^{+0.012} \times 10^{24}$ cm $^{-2}$. A physical picture consistent with this model is that of a patchy or clumpy distribution in which most lines of sight that intercept any material typically have a column density of $N_{H,S}$, but the line-of-sight that is relevant for us happens to have a column density that is a factor of ~ 4 higher than the global average. This could be due to chance fluctuations of material migrating in and out of our line-of-sight, or to a systematic thickening of the distribution towards an equatorial plane that is observed edge-on or close to edge-on. In the former case, fluctuations in the line-of-sight column density should be of the order of the average global column density or less, but in the latter case the fluctuations should be larger than the average global column density. Detailed self-consistent modeling of the Fe $K\alpha$ line and reflection continuum with future monitoring observations with *ASTRO-H* could potentially distinguish between the two scenarios.

(iv) In the above fit with the MYTORUS model, the X-ray reflection continuum originates in Compton-thin matter, and its shape is very different to the “standard” Compton-reflection spectrum from an infinite disc with infinite column density, that is commonly used to fit AGN X-ray spectra. Our fits suggest that the reflected continuum and fluorescent line emission are observed from the back-side of matter on the “far-side” of the distribution, through “holes” on the side closest to the observer.

(v) In our Compton-thin reflection model for Mkn 3, the high-energy spectrum is *not* reflection dominated. Above ~ 10 keV, the reflection continuum is negligible and the spectrum is dominated by the line-of-sight absorption. Therefore the high-energy spectrum is essentially the direct, intrinsic continuum.

(vi) We applied the MYTORUS model described above in two energy bands, ~ 2.4 –45 keV, and ~ 0.5 –45 keV, the latter including additional soft X-ray model components. We obtained consistent results for the global and line-of-sight column densities for both fits. Thus, considering AGN X-ray spectra in general, one could expect to obtain reliable constraints on the line-of-sight and global column densities, at least to a reasonable approximation, without having to consider the often considerable complexities of the soft X-ray spectrum. (However, we note that the relative magnitude of the continuum from distant, optically-thin scattering *is* highly model-dependent.)

(vii) The *Suzaku* data are consistent with a solar abundance of Fe. We note that the Fe abundance cannot trivially be deduced from the magnitude of the discontinuity at the Fe K edge since the “edge-depth” depends on the geometry and column-dependent radiative transfer of continuum photons.

(viii) The MYTORUS model self-consistently calculates the Compton shoulder of the Fe $K\alpha$ and Fe $K\beta$ lines, so it is already included in the model. Our best description of the *Suzaku* data with the MYTORUS model indicates that the matter distribution is globally Compton-thin so the flux of the Compton shoulder is only $\sim 9\%$ of the Fe $K\alpha$ line core and that the data are consistent in detail with the model. In previous works, attempts to reconcile the Fe $K\alpha$ line profile with a Compton-reflection continuum that was assumed to originate in an infinite disc with an infinite column density resulted in the expectation that the ratio of the Compton shoulder flux to that in the line core should be a factor of $\sim 1.5 - 3$ higher than was observed.

(ix) The flux of the Fe $K\beta$ line in the MYTORUS is self-consistently determined by the model and is not adjustable. We obtained an excellent fit to the Fe $K\beta$ line in the data with the decoupled MYTORUS model, despite no empirical adjustments of its flux relative to the Fe $K\alpha$ line.

(x) Our analysis also addresses the “puzzling” lack of correlation between the Fe $K\alpha$ line flux and the magnitude of the Compton-reflection continuum reported by Guainazzi et al. (2012). Their analysis insisted that the reflection continuum is from Compton-thick matter, which forced them to conclude that the Fe $K\alpha$ line originates in a separate Compton-thin medium, whilst the Fe $K\alpha$ line from the Compton-thick matter must be suppressed. However they were not able to offer an explanation for such suppression. Guainazzi et al. (2012) also stated that the reflection continuum from the Compton-thin matter is unobservable. However, they did not fit Compton-thin models of the reflection continuum and Fe $K\alpha$ line to support that assertion. In contrast, we fitted self-consistent models that make no presumptions about the column density of matter producing the reflection continuum and the Fe $K\alpha$ line. We found that the global matter distribution is Compton-thin and its reflection continuum is observable. The situation of a lack of correlation between the Fe $K\alpha$ line flux and Compton-reflection can never arise in analyses using the self-consistent models that we applied because the physical relationship is built in from the outset. We also note that an argument sometimes used to support the assumption of a Compton-thick reflection continuum is the observation of a high infrared to X-ray continuum ratio, and this was also invoked by Guainazzi et al. (2012) for Mkn 3. However, Yaqoob & Murphy (2011a) have shown that the infrared to X-ray ratio is not uniquely determined by the column density of the reprocessor, but has just as important a dependence on its covering factor and on the hardness of the intrinsic X-ray continuum. They further showed that it is possible for a Compton-thin reprocessor to produce an infrared to X-ray ratio that can be comparable to, or actually larger, than that produced by a Compton-thick reprocessor.

Our analysis reveals the important role played by *Compton-thin* X-ray reflection from finite-column-density matter in constraining the average global column density of the matter distribution responsible for producing the narrow Fe $K\alpha$ emission line in AGN. Compton-thin reflection exhibits a richer variety of spectral shapes than the commonly-used, disc-reflection spectrum, which assumes an infinite column density. The X-ray reflection spectrum from finite-column-density material can peak at lower energies than the infinite-column-density counterpart. In Mkn 3, according to the spectral-fitting results with the MYTORUS model, the Compton-thin reflection spectrum is the dominant continuum in the $\sim 3 - 5$ keV band. It is noteworthy that the MYTORUS fit to the Fe $K\alpha$ line, Fe $K\beta$ line, and the Fe K edge region, is so good (see Fig. 5) that there is no suggestion that any more complexity is required, in addition to the mundane, nonrelativistic, physics of the model. The fit in the critical Fe K region was achieved without any free parameters that adjust the Fe $K\alpha$ line, Fe $K\beta$ line, or the Fe K edge with respect to the Compton-reflection continuum.

Our results are also relevant for the study of so-called “changing-look” AGN, which are reported to change from being Compton-thick to Compton-thin, or vice-versa. The phenomenon has commonly been interpreted in terms of transits of clumpy material across the line-of-sight (e.g. Matt, Guainazzi & Maiolino 2003; Risaliti et al. 2010, and references therein), but traditional modeling has been restricted by the assumption that the global matter distribution is Compton-thick. This global distribution contributes an underlying reflection spectrum that is often non-varying whilst the line-of-sight absorption spectrum varies. The possibility that the global matter distribution is Compton-thin then leads to a richer phenomenology that could be observable in changing-look AGN. Indeed, such a case has already been found from a *Suzaku*, *XMM-Newton*, and *Swift* observation campaign of the type 2 AGN, NGC 454 (Marchese et al. 2012). Spectral fitting with the MYTORUS model showed that a Compton-thin reflection component (from a global matter distribution with a column density of $\sim 3 \times 10^{23}$ cm $^{-2}$) remained steady whilst the line-of-sight column density varied between $\sim 10^{23}$ cm $^{-2}$ and $\sim 10^{24}$ cm $^{-2}$. In the “transiting clumps” scenario, no “shutting-down” or “powering up” of the central engine is required to explain the apparent transitions: the average Compton-thin or Compton-thick global matter distribution remains steady over time, only the amount of matter in the line-of-sight fluctuates. This picture is also consistent with the findings of Markowitz, Krumpke, & Nikutta (2014), who investigated the properties of transient absorption events in AGN, leading to constraints on clumpy torus models of the circumnuclear matter distribution. In the transiting clump model of spectral variability, changing-look AGN are not members of a special class of AGN. Rather, they are a loosely defined subset of AGN in which the difference between the line-of-sight and global column densities happens to be large enough to cause transitions between two “extremal” spectral states, one that is Compton-thick and the other Compton-thin. Other AGN, which may constitute a majority, in which the contrast between the line-of-sight and global column densities is less severe, would exhibit more moderate spectral variability, insufficient to classify them as changing-look AGN. Nevertheless, the transiting matter interpretation of changing-look AGN cannot be universal, as LaMassa et al. (2015) have presented a detailed multiwaveband study of a type 1 quasar to type 1.9 AGN transition that cannot be explained by variable line-of-sight absorption, but instead is attributed to variable ionization of the matter surrounding the central source.

The clumpy nature of the torus that is increasingly becoming apparent from X-ray observations has also been inferred from theoretical work on the infrared properties of AGN (e.g. Elitzur 2008; Nenkova et al. 2008, 2010). In particular, Nenkova et al. (2008) note that observations imply a clumpy medium because it can produce “isotropic infrared emission but highly anisotropic obscuration.” Nevertheless, it has been argued by Feltre et al. (2012), based on a detailed study of smooth and

clumpy models, that ambiguities still exist because the two types of model depend on very different assumptions. Regardless of the clumpiness of the X-ray reprocessor, it will be important to determine for a larger sample of type 2 AGN, how common it is for the mean global column density of the X-ray reprocessor to be very different to the line-of-sight column density. Traditionally, simplistic, one-dimensional models have been fitted to derive column densities, with the implicit assumption that the global column density is the same as the line-of-sight column density. Whether or not this is the case clearly has implications for the energy budget for reprocessing X-rays into infrared emission, and for population synthesis models of the cosmic X-ray background.

Acknowledgments

The authors acknowledge support for this work from NASA grants NNX09AD01G, NNX10AE83G, and NNX14AE62G. This research has made use of data and software provided by the High Energy Astrophysics Science Archive Research Center (HEASARC), which is a service of the Astrophysics Science Division at NASA/GSFC and the High Energy Astrophysics Division of the Smithsonian Astrophysical Observatory.

This paper has been produced using the Royal Astronomical Society/Blackwell Science L^AT_EX style file.

REFERENCES

- Akylas A., Georgantopoulos I., Nandra K., 2006, AN, 327, 1091
 Anders E., Grevesse N., 1989, Geochimica et Cosmochimica Acta 53, 197
 Antonucci R. R. J., 1993, ARA&A, 31, 473
 Antonucci R. R. J., Miller, J. S., 1985, ApJ, 297, 621
 Arnaud K. A., 1996, in Astronomical Data Analysis Software and Systems V, ed. Jacoby, G., Barnes, J. (Astronomical Society of the Pacific), Conference Series, Vol. 101, p. 17
 Awaki, H. et al., 2008, PASJ, 60, 293
 Bearden J. A., 1967, Rev. Mod. Phys., 39, 78
 Bianchi S., Miniutti G., Fabian A. C., Iwasawa K., 2005, MNRAS, 360, 380
 Brandl B. R. et al., 2006, ApJ, 653, 1129
 Brandl B. R. et al., 2007, ApJ, 665, 884
 Brightman M., Nandra K., 2011, MNRAS, 413, 1206 (BN11)
 Brightman M. et al., 2015, ApJ, 805, 41
 Cappi M. et al., 1999, A&A, 344, 857
 Colbert E. J. M., Ptak A. F., 2002, ApJS, 143, 25
 Dadina M., 2007, A&A, 461, 1209
 Dadina M., 2008, A&A, 485, 417
 Elitzur M., 2008, NewAR, 52, 274
 Feltre A., Hatziminaoglou E., Fritz J., Franceschini A., 2012, MNRAS, 426, 120
 Fukazawa Y., et al., 2011, ApJ, 727, 19
 Georgantopoulos I. et al., 2011, A&A, 534, 23
 George I. M., Fabian A. C. 1991, MNRAS, 249, 352
 Gilli R., Comastri A., Hasinger G., 2007, A&A, 463, 79
 Griffiths R. G., Warwick R. S., Georgantopoulos I., Done C., Smith D. A., MNRAS, 298, 1159
 Guainazzi M., La Parola V., Miniutti G., Segreto A., Longinotti A. L. 2012, A&A, 547, 31
 Ikeda S., Awaki H., Terashima Y., 2009, ApJ, 692, 608
 Iwasawa K., Yaqoob T., Awaki H., Ogasaka Y., 1994, PASJ, 46, L167
 Koyama K., et al., 2007, PASJ, 59, 23
 Laha S., Guainazzi M., Dewangan G. C., Chakravorty, S., Kembhavi A. K. 2014, MNRAS, 441, 2613
 LaMassa S. M., Yaqoob T., Ptak A., Jianjun J., Heckman T. M., Gandhi P., Urry C. M., 2014, ApJ, 787, 61
 LaMassa S. M. et al., 2015, ApJ, 800, 144
 Liu Y., Li X., 2014, ApJ, 787, 52
 Liu Y., Li X., 2015, MNRAS, 448, L53
 Marchese E., Braitto V., Della Ceca R., Caccianiga A., Severgnini, P., 2012, MNRAS, 421, 1803
 Markowitz A., Krumpel M., Nikutta R., 2014, MNRAS, 439, 1403
 Matt G., 2002, MNRAS, 337, 147
 Matt G., Guainazzi M., Maiolino R., 2003, MNRAS, 342, 422
 Miller J. S., Goodrich R. W., 1990, ApJ, 355, 456
 Mitsuda K. et al., 2007, PASJ, 59, 1
 Morse J. A., Wilson A. S., Elvis M., Weaver K. A. 1995, ApJ, 439, 121
 Murphy K. D., Yaqoob T., 2009, MNRAS, 397, 1549
 Nenkova M., Sirocky M. M., Nikutta R., Ivezić Ž., Elitzur, M., 2008, ApJ, 685, 160
 Nenkova M., Sirocky M. M., Nikutta R., Ivezić Ž., Elitzur, M., 2010, ApJ, 723, 1827
 Netzer H. 1990, in Active Galactic Nuclei, ed. R. D. Blandford, H. Netzer, L. Woltjer (Berlin: Springer), 137
 Risaliti G., Elvis M., Bianchi S., Matt G., 2010, MNRAS, 406, L20
 Shu X. W., Yaqoob T., Wang J. X., 2011, ApJ, 738 147

- Serlemitsos P. J. et al., 2007, PASJ, 59, 9
Takahashi T., et al., 2007, PASJ, 59, 35
Tatum M. M., Turner T. J., Miller L., Reeves J. N., 2013, ApJ, 762, 80
Tift W. G., Cocke W. J., 1988, ApJS, 67, 1
Tran H. D., ApJ, 440, 565
Turner T. J., George I. M., Nandra K., Mushotzky R. F. 1997, ApJ, 488, 164
Turner T. J., Urry C. M., Mushotzky R. F., 1993, ApJ, 418, 653
Sako M., Kahn S., Paerels F., Liedahl D. A., 2000, ApJ, 543, L115
Stark A. A., Gammie C. F., Wilson R. W., Bally J., Linke R., Heiles C., Hurwitz M., 1992, ApJS, 79, 77
Ueda Y., Akiyama M., Hasinger G., Miyaki T., Watson M., 2014, ApJ, 786, 104
Urry C. M., Padovani P., 1995, PASP, 107, 803
Vasudevan R. V., Fabian A. C., Gandhi P., Winter L. M., Mushotzky R. F., 2010, MNRAS, 402, 1081
Verner D. A., Ferland G. J., Korista K. T., Yakovlev D. G., 1996, ApJ, 465, 487
Woo J. H., Urry C. M. 2002, ApJ, 579, 530
Yaqoob T., 2012, MNRAS, 423, 3360
Yaqoob T., Murphy K. D., 2010, MNRAS, 412, 277
Yaqoob T., Murphy K. D., 2011a, MNRAS, 412, 835
Yaqoob T., Murphy K. D., 2011b, MNRAS, 412, 1765